GEOSPHERE

GEOSPHERE, v. 18, no. 2

https://doi.org/10.1130/GES02437.1

10 figures; 1 table; 1 set of supplemental files

CORRESPONDENCE: markschmitz@boisestate.edu

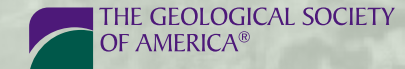
CITATION: Isakson, V.H., Schmitz, M.D., Dehler, C.M., Macdonald, F.A., and Yonkee, W.A., 2022, A robust age model for the Cryogenian Pocatello Formation of southeastern Idaho (northwestern USA) from tandem in situ and isotope dilution U-Pb dating of volcanic tuffs and epiclastic detrital zircons: Geosphere, v. 18, no. 2, p. 825–849, https://doi.org/10.1130/GES02437.1.

Science Editor: Shanaka de Silva Associate Editor: Todd A. LaMaskir

Received 21 March 2021 Revision received 9 July 2021 Accepted 28 December 2021

Published online 18 February 2022





This paper is published under the terms of the CC-BY-NC license.

© 2022 The Authors

A robust age model for the Cryogenian Pocatello Formation of southeastern Idaho (northwestern USA) from tandem in situ and isotope dilution U-Pb dating of volcanic tuffs and epiclastic detrital zircons

Vincent H. Isakson¹, Mark D. Schmitz¹, Carol M. Dehler², Francis A. Macdonald³, and W. Adolph Yonkee⁴

- ¹Department of Geosciences, Boise State University, 1910 University Drive, Boise, Idaho 83725, USA
- ²Department of Geology, Utah State University, 4505 Old Main Hill, Logan, Utah 84322, USA
- ³Department of Earth Science, University of California, Santa Barbara, California 93106, USA
- ⁴Department of Earth and Environmental Sciences, Weber State University, Odgen, Utah 84408, USA

ABSTRACT

Tandem in situ and isotope dilution U-Pb analysis of zircons from pyroclastic volcanic rocks and both glacial and non-glacial sedimentary strata of the Pocatello Formation (Idaho, northwestern USA) provides new age constraints on Cryogenian glaciation in the North American Cordillera. Two dacitic tuffs sampled within glacigenic strata of the lower diamictite interval of the Scout Mountain Member yield high-precision chemical abrasion isotope dilution U-Pb zircon eruption and depositional ages of 696.43 ± 0.21 and 695.17 ± 0.20 Ma. When supplemented by a new high-precision detrital zircon maximum depositional age of ≤670 Ma for shoreface and offshore sandstones unconformably overlying the lower diamictite, these data are consistent with correlation of the lower diamictite to the early Cryogenian (ca. 717-660 Ma) Sturtian glaciation. These 670-675 Ma zircons persist in beds above the upper diamictite and cap dolostone units, up to and including a purported "reworked fallout tuff," which we instead conclude provides only a maximum depositional age of ≤673 Ma from epiclastic volcanic detritus. Rare detrital zircons as young as 658 Ma provide a maximum depositional age for the upper diamictite and overlying cap dolostone units. This new geochronological framework supports litho- and chemostratigraphic correlations of the lower and upper diamictite intervals of the Scout Mountain Member of the Pocatello Formation with the Sturtian (716–660 Ma) and Marinoan (≤650–635 Ma) low-latitude glaciations, respectively. The Pocatello Formation thus contains a more complete record of Cryogenian glaciations than previously postulated.

■ INTRODUCTION

Neoproterozoic (Cryogenian) glacial successions are present worldwide and are interpreted to record global "snowball Earth" glaciations (Kirschvink, 1992;

Mark Schmitz https://orcid.org/0000-0003-2888-0321

Hoffman et al., 2017). The snowball Earth hypothesis originated from energy-balance models and an understanding of the bounds of the silicate-weathering and ice-albedo climate feedbacks (Budyko, 1969; North et al., 1981, Walker et al., 1981). These ideas were applied to the Neoproterozoic glacial record as sedimentological and paleomagnetic evidence within these deposits revealed grounded marine ice sheets at low latitude (Evans, 2000; Evans and Raub, 2011) and the global, intimate association of ice-proximal deposits with distinctive sharply overlying warm-water cap dolostones (Williams, 1979; Hoffman et al., 1998). The latter have been interpreted to record the rapid precipitation of calcium carbonate from oversaturated oceans driven by a weathering-derived alkalinity flux during sea-level rise in the greenhouse aftermath of global deglaciation (Hoffman and Schrag, 2002; Hoffman et al., 2011).

A fundamental tenet of the snowball Earth hypothesis is the global synchrony and rapidity of low-latitude glaciation and deglaciation (Kirschvink, 1992; Hoffman and Schrag, 2002). At least two Cryogenian low-latitude glaciations are generally recognized: the earlier Sturtian and the later Marinoan (Hoffman and Schrag, 2002; Hoffman and Li, 2009; Rooney et al., 2015), which are both associated with cap carbonate units displaying distinctive lithological and isotopic characteristics such as seafloor crystal fans and negative δ^{13} C excursions, respectively (Hoffman et al., 2011). Complete sections of the Sturtian or Marinoan glacial sequences are rare due to erosional and structural omissions, and lithostratigraphic correlations are further complicated by syn-sedimentary tectonism associated with the protracted break-up of Rodinia (Li et al., 2008; Macdonald et al., 2013a). Moreover, many Cryogenian stratigraphic sections lack dateable material. Consequently, the number, timing, and duration of these glacial episodes are debated (Kennedy et al., 1998; Lund et al., 2003; Fanning and Link, 2008; Kendall et al., 2009; Macdonald et al., 2013a; Rooney et al., 2015).

Nonetheless, integrated geological and geochronological studies of the past decade are providing an increasingly robust chronostratigraphic framework for the Cryogenian glaciations. The onset of the Sturtian glaciation is constrained

between 717.4 \pm 0.2 and 716.9 \pm 0.4 Ma with U-Pb zircon geochronology (unless otherwise noted, all references to U-Pb geochronology utilize the $^{206}\text{Pb/z}^{238}\text{U}$ decay chain) using chemical abrasion–isotope dilution thermal ionization mass spectrometry (CA-IDTIMS) on volcanic rocks below (Mount Harper volcanics) and within (Eagle Creek Formation) glacial deposits of the Rapitan Group in the Coal Creek inlier of Yukon, Canada (Macdonald et al., 2010, 2018). This age is consistent with the onset of the Sturtian glaciation in South China, where a volcaniclastic unit directly below the lowermost Chang'an Formation yielded a maximum depositional age by U-Pb zircon geochronology using CA-IDTIMS of 720.2 \pm 1.4 Ma (Lan et al., 2020), and in Arctic Alaska, where volcaniclastic strata directly below the Hula Hula diamictite have yielded a 719.5 \pm 0.3 Ma (CA-IDTIMS) maximum depositional age (Cox et al., 2015). Similarly, two tuff horizons below the glacial diamictite in the Tambien Group of Ethiopia have yielded eruption ages of 719.7 \pm 0.5 Ma (MacLennan et al., 2018).

Some commonly cited U-Pb zircon ages for rocks interpreted to be syn-Sturtian include a 711.5 ± 0.3 Ma (IDTIMS) eruption age for a tuffaceous bed near the base of the Gubrah Formation in Oman (Bowring et al., 2007); 705.4 ± 0.3 Ma volcanics from the syn-glacial Limekiln Spring Member of the Kingston Peak Formation in Death Valley, California, USA (Nelson et al., 2020); 696.2 ± 0.2 to 690.1 ± 0.2 Ma (CA-IDTIMS) eruption ages for various volcanic rocks of Gataga volcanics of northern British Columbia (Eyster et al., 2018); a 709 ± 5 Ma (sensitive high-resolution ion microprobe, or SHRIMP; Fanning and Link, 2004) maximum depositional age, later revised to 686 ± 4 Ma (SHRIMP; Fanning and Link, 2008) and 687.4 ± 1.3 Ma (CA-IDTIMS; Condon and Bowring, 2011), for tuffaceous breccia in the lower Scout Mountain Member of the Pocatello Formation in southeastern Idaho, northwestern USA; a 685.5 ± 0.4 Ma (CA-IDTIMS) maximum depositional age for a volcaniclastic diamictite in the lower Scout Mountain Member of the Pocatello Formation (Keeley et al., 2013): 685 ± 7 and 684 ± 4 Ma (SHRIMP) eruption ages for rhyodacite flows from the Edwardsburg Formation of central Idaho (Lund et al., 2003); and a 663.0 ± 0.1 Ma U-Pb zircon eruption age (CA-IDTIMS) for a tuff horizon interbedded with diamictite in the Wilyerpa Formation in South Australia (Cox et al., 2018).

Age constraints on the termination of the Sturtian glaciation include a 662.4 \pm 3.9 Ma (Re-Os) depositional age from carbonaceous shale just above the cap dolostone at the base of the Twitya Formation in the Mackenzie Mountains of Canada (Rooney et al., 2014); a 662.9 \pm 4.3 Ma ($^{207}\text{Pb}/^{206}\text{Pb}$; IDTIMS) U-Pb zircon eruption age on a tuffaceous bed within the condensed "rhodochrosite" in the post-glacial Datangpo Formation of the Zhailanggou section, eastern Guizhou, South China (Zhou et al., 2004); 659.3 \pm 2.4 and 657.3 \pm 3.2 Ma (SHRIMP) U-Pb zircon eruption ages for two tuffs from the base of the Datangpo Formation in the Jiangjunshan section, northeastern Guizhou, South China (Wang et al., 2019); a 659.0 \pm 4.5 Ma (Re-Os) depositional age from carbonaceous shale within the cap dolostone directly above the Maikhan-Uul diamictite in Mongolia (Rooney et al., 2015); and a 657.2 \pm 5.4 Ma (Re-Os) depositional age from carbonaceous shale at the base of the post-glacial Aralka Formation, Australia (Kendall et al., 2006). Most recently, Zhou et al. (2019) reported a CA-IDTIMS U-Pb zircon eruption age of 658.8 \pm 0.5 Ma for a tuff bed in the basal Datangpo Formation,

South China, and Rooney et al. (2020) reported three U-Pb zircon eruption ages (CA-IDTIMS) of 660.98 ± 0.74 Ma, 658.97 ± 0.76 Ma, and 657.17 ± 0.78 Ma from the lower Datangpo Formation and a Re-Os date of 660.6 ± 3.9 Ma from within the uppermost unit of a diamictite below the Datangpo Formation.

Although these accumulating geochronological data can be interpreted to support the global synchrony and rapidity of Sturtian ice-sheet initiation and deglaciation, this remarkably long ~56 m.y. time span, combined with possible issues regarding the interpretation of glacial affinity in tectonically active environments (false positives) and in quiet environments below a stable ice-grounding line (false negatives), stratigraphic context, and/or interpretation of isotopic dates themselves have raised questions regarding the regional and global correlation of Sturtian glacial deposits as well as the possible subdivision of the Sturtian glaciation into multiple discrete glaciations (e.g., Fanning and Link, 2008; Lan et al., 2015; Spence et al., 2016; Le Heron et al., 2020) versus the plausibility of a prolonged Sturtian glaciation lasting from ca. 717 Ma to ca. 661 Ma (Rooney et al., 2014, 2015, 2020).

Maximum age constraints for the Marinoan glaciation come from pre-glacial deposits in South China, Death Valley, and Australia: a 654.5 \pm 3.8 Ma (SHRIMP) U-Pb zircon eruption age for an ash bed 0.6 m below the Nantuo glacial diamictite in shale of the upper Datangpo Formation (Zhang et al., 2008) subsequently redated by CA-IDTIMS methods to 657.2 \pm 0.8 Ma (Rooney et al., 2020); a 651.7 \pm 0.6 Ma (CA-IDTIMS) U-Pb zircon maximum depositional age for the nonglacial Thorndike submember, which is below the Wildrose diamictite submember of the South Park Member, Kingston Peak Formation of Death Valley, California, USA (Nelson et al., 2020); and a Re-Os isochron black shale depositional age of 643 \pm 2.4 Ma for the basal Tindelpina Shale Member of the Tapley Hill Formation in Australia (Kendall et al., 2006). The Marinoan onset has also been estimated to be \leq 650 Ma using cyclostratigraphic analyses on the Datangpo Formation (Bao et al., 2018).

Syn-glacial U-Pb zircon age constraints on the Marinoan episode include a 639.3 ± 0.3 Ma (CA-IDTIMS) eruption age for an ash bed in glaciomarine deposits of the Ghaub Formation in Namibia (Prave et al., 2016); a 636.4 ± 0.5 Ma (CA-IDTIMS) maximum depositional age for a volcaniclastic unit in the glacial strata–to–cap dolostone transition in Tasmania (Calver et al., 2013); a 636.3 ± 4.9 Ma (SHRIMP) eruption age for a fallout tuff from the Nantuo Formation in South China (Zhang et al., 2008); a 634.6 ± 0.9 Ma (CA-IDTIMS) eruption age from a tuffaceous mudstone in the Nantuo Formation (Zhou et al., 2019); and a 635.2 ± 0.6 Ma (CA-IDTIMS) eruption age for a tuff bed in the Navachab Formation diamictite in the Swakop terrane of Namibia (Hoffmann et al., 2004; Prave et al., 2016). The end of the Marinoan glacial episode is marked by a 635.2 ± 0.6 Ma (CA-IDTIMS) volcanic ash layer within the cap dolostone of the Doushantuo Formation in South China (Condon et al., 2005). These data indicate that Marinoan glaciation had a duration >4 m.y. and possibly as long as ~15 m.y.

The Neoproterozoic rock record of northern Utah and southeastern Idaho (western USA) includes pre-, syn- and post-glacial Cryogenian strata (Crittenden et al., 1971; Link et al., 1993; Yonkee et al., 2014). Diamictite-bearing strata within the Pocatello Formation of southeastern Idaho and correlative Perry Canyon

Formation in northern Utah were previously recognized to record two distinct glacigenic successions separated by an interval of non-glacigenic marine deposition (Crittenden et al., 1983; Balgord et al., 2013). Based upon the 667 ± 5 Ma U-Pb zircon age of a "reworked fallout tuff bed" (Fanning and Link, 2004) in the uppermost Scout Mountain Member of the Pocatello Formation (Fig. 1), above the upper diamictite and cap dolostone, both of these glacial intervals have been interpreted as Sturtian in age (Fanning and Link, 2004; Link and Christie-Blick, 2011; Yonkee et al., 2014), challenging the notion of a single, long-lived Sturtian snowball Earth. On the other hand, interpretation of the U-Pb zircon ages in these rocks has been shown to be complex (Condon and Bowring, 2011; Keeley et al., 2013), and consequently correlations with other Neoproterozoic glacial deposits remain uncertain (Lund et al., 2003; Fanning and Link, 2008; Dehler et al., 2011; Macdonald et al., 2013a; Yonkee et al., 2014; Lan et al., 2015). A prominent example is the distinctive lithology and chemostratigraphy of the cap dolostone associated with the upper diamictite unit, which has prompted correlation to the ca. 635 Ma basal Ediacaran cap carbonates both regionally and globally (e.g., Dehler et al., 2011; Petterson et al., 2011; Macdonald et al., 2013a).

Central to this uncertainty are the precision and accuracy of the techniques used for determining the age of the diamictites and related deposits. Microbeam techniques are typically limited to a precision no better than 2% for an individual analysis. This equates to an uncertainty of ±14 m.y. from a ca. 700 Ma sample, which encompasses half of the ~56 m.y. Sturtian glacial epoch, or ±13 m.y. from a ca. 640 Ma sample, which covers the Marinoan glacial epoch in its entirety. The relatively low precision of an individual analysis may be overcome by pooling large-n analyses of normally distributed dates into a weighted mean, reducing statistical uncertainty in the model age. However, this strategy precludes the detection of subtle Pb loss (producing a younger age bias) or the identification of a mixed sample of epiclastic detrital zircon crystals (leading to misidentification as a volcanic deposit), both of which limit the development of accurate age models (Condon and Bowring, 2011). By contrast, high-precision CA-IDTIMS U-Pb dates can provide a more highly resolved and robust age model for the succession and improve the foundation for regional correlation of purportedly equivalent units. To this end, we present tandem laser ablation-inductively coupled plasma mass spectrometry (LA-ICPMS) and high-precision CA-IDTIMS U-Pb dates on the same zircon crystals from samples of volcanic rock and glacigenic and non-glacigenic sedimentary strata from the Pocatello Formation. The procedures used in this study highlight the ability of this tandem workflow to first allow rapid screening of zircon crystals for identification of their provenance and efficient isolation of the youngest mode with an in situ microbeam technique, and then allow resolution of issues related to Pb loss (Mattinson, 2005) and the recognition of epiclastic detrital zircon crystals of diverse (Cryogenian) age inherent to the deposits (Condon and Bowring, 2011) with high-precision CA-IDTIMS analysis. Our new high-resolution dates significantly revise the age model for the Pocatello Formation; specifically, they allow us to establish more accurate syn-depositional and maximum depositional age constraints on glacigenic strata, refute previous minimum age constraints on glaciation (Fanning and Link, 2004; Link and Christie-Blick, 2011), and affirm the high probability that both Sturtian and Marinoan glacial strata are preserved within the Cryogenian stratigraphy of southeastern Idaho.

■ BACKGROUND

The Pocatello Formation

Neoproterozoic rocks of southeastern Idaho and northern Utah formed within extensional basins as part of the multi-phased Rodinian supercontinent breakup that culminated with the development of a passive continental margin extending from eastern Alaska to California by ca. 540 Ma (e.g., Bond et al., 1983; Ross, 1991; Levy and Christie-Blick, 1991; Lund et al., 2003; Dickinson, 2006; Colpron et al., 2002; Macdonald et al., 2013b; Fedo and Cooper, 2001; Yonkee et al., 2014; Moynihan et al., 2019) (Fig. 1). Commonly correlated glacial deposits in the region include the Pocatello and Edwardsburg Formations in Idaho and the Mineral Fork Formation, Perry Canyon Formation, Horse Canyon Formation, Sheeprock Group, and Trout Creek sequence in Utah (e.g., Crittenden et al., 1983; Christie-Blick, 1983; Link et al., 1993; Balgord et al., 2013; Yonkee et al., 2014). Regional exposures are mostly located within the western thrust system of the Sevier fold-and-thrust belt. Thrust sheets associated with these exposures belong to the Willard-Paris-Putnam fault system of northern Utah and southeastern Idaho and the Tintic-Sheeprock-Canyon Range fault system of west-central Utah (Link and Christie-Blick, 2011, and references therein). The Pocatello Formation is cut by strike-slip and low- and high-angle dip-slip faults, including the Portneuf Narrows fault, which separates overturned rocks on the north side of Portneuf Narrows from right-side-up equivalents to the south (Fig. 2).

The greenschist facies Pocatello Formation is an ~1.5-km-thick package of dominantly siliciclastic, lesser volcanic, and rare carbonate rocks exposed in the Pocatello and Bannock Ranges (Fig. 1) of southeastern Idaho and northern Utah (Link et al., 1993; Link and Christie-Blick, 2011; Dehler et al., 2011). The structural panel comprising these ranges was transported eastward ~100 km in the Mesozoic along the Paris-Willard thrust fault and was subsequently exposed via regional normal faulting during Basin and Range extension (Link, 1983; Yonkee et al., 2014). The Pocatello Formation is composed of three members: the Bannock Volcanic Member (type section on the west side of China Peak, east of Pocatello), the Scout Mountain Member (type section on the west side and the ridgeline of Scout Mountain), and the informal upper member (type section southeast of Scout Mountain) (Link, 1983; Crittenden et al., 1971) (Fig. 1).

The Bannock Volcanic Member comprises mafic metavolcanic and volcanic clastic rocks and has a minimum thickness of 200–450 m (Fig. 1); the base is not exposed, and the upper part interfingers with the overlying Scout Mountain Member (Link, 1983). The volcanic rocks are tholeitic-alkaline to alkaline basalts and are interpreted to be the products of intra-plate rift volcanism (Harper and Link, 1986; Keeley and Link, 2011). Felsic volcanic clasts within the overlying Scout Mountain Member represent the felsic component of bimodal volcanism

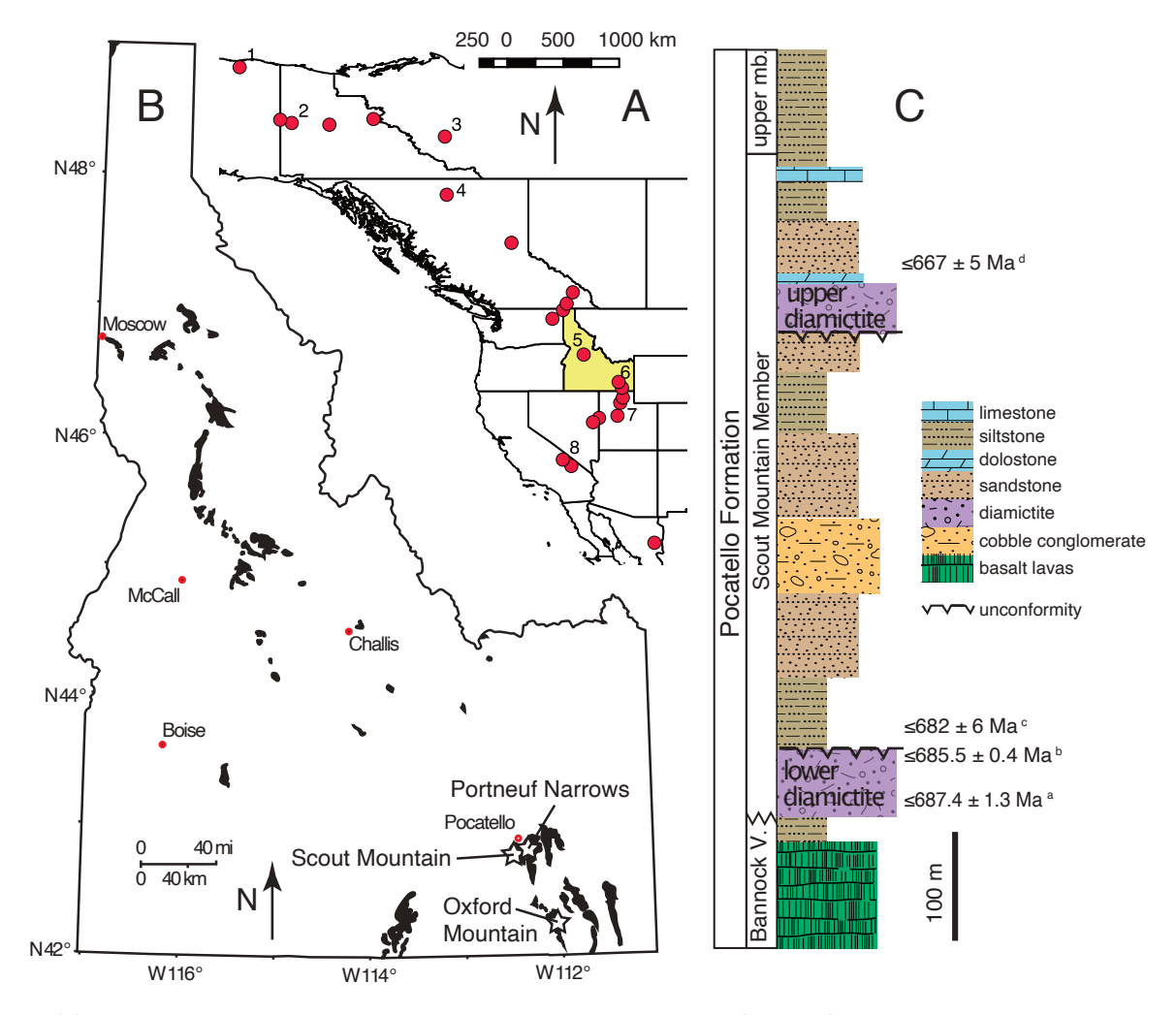


Figure 1. (A) Locations of diamictite-bearing successions along the North American Cordillera (red circles) with numbered locations referred to in text: 1—Hula Hula diamictite in Arctic Alaska (Cox et al., 2015); 2—Eagle Creek diamictite in the Coal Creek inlier of Yukon, Canada (Macdonald et al., 2010, 2018); 3—Rapitan Group in the Mackenzie Mountains of Canada (note that the distribution is much more extensive along the belt than shown with the single point; Rooney et al., 2014); 4—Gataga volcanics of northern British Columbia, Canada (Eyster et al., 2018); 5—Edwardsburg Formation of central Idaho, USA (Lund et al., 2003); 6—Pocatello Formation of southeastern Idaho (this paper); 7—Perry Canyon Formation in northern Utah, USA (Crittenden et al., 1983); 8—Kingston Peak Formation in the Panamint Range of southeastern California, USA (Nelson et al., 2020). (B) Outcrop belt of Neoproterozoic Windermere Supergroup and coeval plutonic rocks in Idaho, including the locations of Pocatello Formation outcrops discussed in this paper. (C) Simplified stratigraphy of the Pocatello Formation with previous age constraints: a—≤709 ± 5 Ma (SHRIMP; Fanning and Link, 2004), later revised to ≤686 ± 4 Ma (SHRIMP; Fanning and Link, 2004) and ≤687.4 ± 1.3 Ma (CA-IDTIMS; Condon and Bowring, 2011) maximum depositional age for tuffaceous breccia in the lower Scout Mountain Member of the Pocatello Formation in southern Idaho; b—≤685.5 ± 0.4 Ma (CA-IDTIMS) maximum depositional age for a volcanic diamictite in the lower Scout Mountain Member of the Pocatello Formation (Keeley et al., 2013); c—≤682 ± 6 Ma (SHRIMP) detrital zircon age from above the upper diamictite (Fanning and Link, 2004). V.—Volcanic Member; mb.—member.

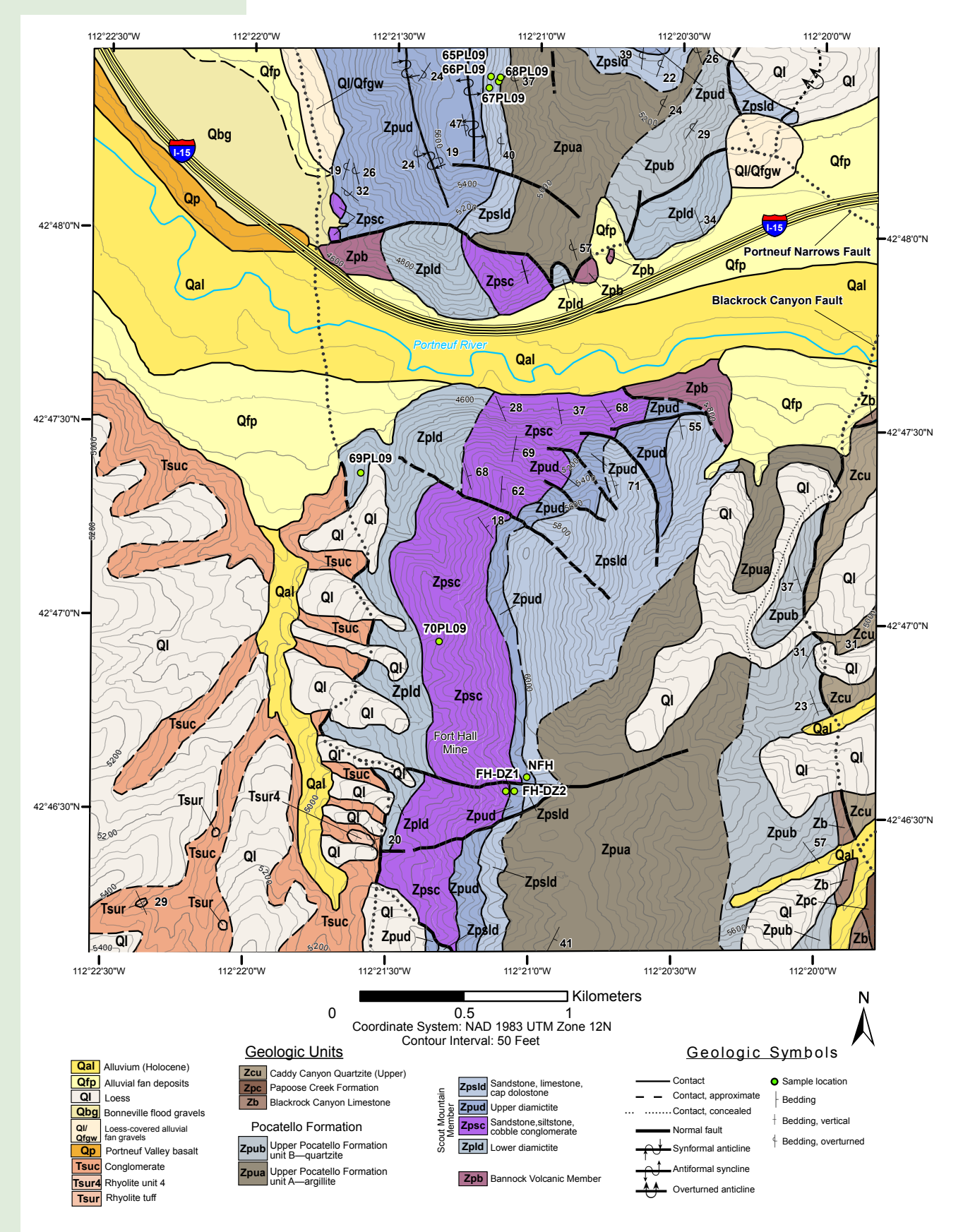


Figure 2. Geologic map of the Portneuf Narrows area of southeastern Idaho, modified from Rodgers et al. (2006), showing sample locations of this study (green circles). NAD 1983—North American Datum of 1983; UTM—Universal Transverse Mercator.

within the Bannock Volcanic Member (Fanning and Link, 2004). Basalt flows are locally interbedded within the lower Scout Mountain Member, providing evidence that the transition between the two members may be conformable (Keeley and Link, 2011; Keeley et al., 2013).

A variety of lithologies compose the ~800-m-thick Scout Mountain Member (Link, 1982) (Fig. 1), which we divide into the following informal units in the Portneuf Narrows (and Scout Mountain) area(s): lower diamictite, arkosic sandstone, siltstone, cobble conglomerate, upper diamictite, cap dolostone, and upper sandstone and limestone (Figs. 2, 3, 4). The base of the member is composed of thinly bedded siltstone with dark mudstone rip-up clasts interbedded with matrix-supported diamictite that contains quartzite, mafic and felsic volcanic, phyllite, and granitoid clasts, some of which are glacially faceted and striated. This "lower diamictite" is overlain by cross-bedded and massive arkosic sandstone, thinly bedded siltstone, polymict cobble conglomerate, and a polymict "upper diamictite". The cobble conglomerate and upper diamictite contain granitic, gneissic, guartzitic, and felsic volcanic clasts, with glacial striations found on faceted clasts in the upper diamictite (Link, 1982). Overlying the upper diamictite is a pink to buff-colored laminated dolostone with interbedded sandstone and argillite that culminates with limestone beds containing replaced aragonite crystal fans (Lorentz et al., 2004; Dehler et al., 2011). The lateral extent (>100 km), correlation with glacial deposits to the south (e.g., Perry Canyon and Mineral Fork Formations; Crittenden et al., 1983; Balgord et al., 2013), and occasional striated and faceted clasts indicate a glacial origin for the diamictite units (e.g., Crittenden et al., 1983; Link et al., 1994; Yonkee et al. 2014). As a whole, the Scout Mountain Member is interpreted to record deposition of continent-derived immature to mature subaqueous sediments containing reworked glacigenic sediments (Crittenden et al., 1983; Link et al., 1994), representing two phases of the ca. 717-661 Ma Sturtian glaciation (Fanning and Link, 2004, 2008; Yonkee et al., 2014). In contrast, based upon the distinctive lithology and chemostratigraphy of the overlying cap dolostone, others have correlated the upper diamictite unit with the ≤650-635 Ma Marinoan glaciation (e.g., Dehler et al., 2011; Petterson et al., 2011; Macdonald et al., 2013a). The Scout Mountain Member grades into the >600 m informal upper member of the Pocatello Formation, which comprises laminated argillite and quartzite (Link, 1982). Facies above the upper diamictite and cap dolostone represent shoreface and deeper-water conditions interpreted to be the result of post-glacial eustatic sea-level rise (Link, 1983; Link et al., 1994; Dehler et al., 2011).

Previous Geochronology of the Pocatello Formation

Radioisotopic age determinations for the Pocatello Formation have proven to be problematic. Fanning and Link (2004) reported a U-Pb zircon SHRIMP date of 717 \pm 4 Ma from a rhyolitic clast within the upper diamictite at Portneuf Narrows, which they later revised to 701 \pm 4 Ma (Fanning and Link, 2008). Additionally, they reported a U-Pb zircon SHRIMP date of 709 \pm 5 Ma from an

epiclastic tuff breccia some 50 m below the highest exposure of lower diamictite at Oxford Mountain (Fig. 4), later revised to 686 ± 4 Ma (Fanning and Link, 2008) with the acknowledgment that the stratigraphic position was not well constrained due to extensive faulting within the section.

Condon and Bowring (2011) re-evaluated the original Oxford Mountain epiclastic tuff breccia sample of Fanning and Link (2004) along with a recollected equivalent sample and found a multimodal epiclastic detrital signal using high-precision CA-IDTIMS U-Pb zircon analysis. Condon and Bowring (2011) concluded that the relatively low precision of individual SHRIMP spot analyses (precision >1%) lacked the resolution to identify heterogeneous epiclastic crystal ages and assigned a maximum depositional age of 687 \pm 1.3 Ma on the basis of the youngest single CA-IDTIMS date.

The conclusion of Condon and Bowring (2011) was reconfirmed in a subsequent investigation by Keeley et al. (2013). The authors described a suite of siliciclastic and volcaniclastic facies within the Oxford Mountain tuffite, including the "epiclastic tuff breccia" of Fanning and Link (2004, 2008) and Condon and Bowring (2011), interbedded and in gradational contact with the lower diamictite of the Scout Mountain Member. CA-IDTIMS analyses of five different tuffite samples identified a range of crystal ages from ca. 685 Ma to ca. 709 Ma (Keeley et al., 2013), which were interpreted to represent epiclastic detritus from protracted regional volcanism. A youngest weighted mean date of 685.5 ± 0.4 Ma for 10 grains from one sample of volcaniclastic diamictite with cobble-sized volcanic clasts high in the exposed lower diamictite section provided a maximum depositional age for any overlying units. Keeley et al. (2013) correlated the source of this 685.5 ± 0.4 Ma detritus with U-Pb zircon (SHRIMP) ages of 686 ± 7 and 685 ± 4 Ma for volcanic rocks of the Edwardsburg Formation in central Idaho (Lund et al., 2003).

Stratigraphic Sections and Samples

Portneuf Narrows

The stratigraphic sections on the north and south sides of Portneuf Narrows (Fig. 2) have been extensively described by Link (1982), Keeley et al. (2013), Dehler et al. (2011), and Yonkee et al. (2014). We collected a volcanic-rich diamictite sample (69PL09) from the lowest exposure of the lower diamictite unit on the south side of Portneuf Narrows at the same location as sample 62JK09 of Keeley et al. (2013). An arkosic sandstone sample (70PL09) was collected from ~20 m above the underlying lower diamictite and is equivalent to the plagioclase-arkose sample (15PL08) of Keeley et al. (2013). Three samples of the upper diamictite and one sample of cap dolostone were sampled in a detailed traverse across the contact at the Fort Hall section of Dehler et al. (2011), and a single sample of cap dolostone was collected from the North Fort Hall section of Dehler et al. (2011). We also extracted zircons for CA-IDTIMS analysis from samples of upper diamictite (FH-DZ1) and cap dolostone (FH-DZ2) from the Fort Hall section discussed in Yonkee et al. (2014) and Dehler et al. (2009).

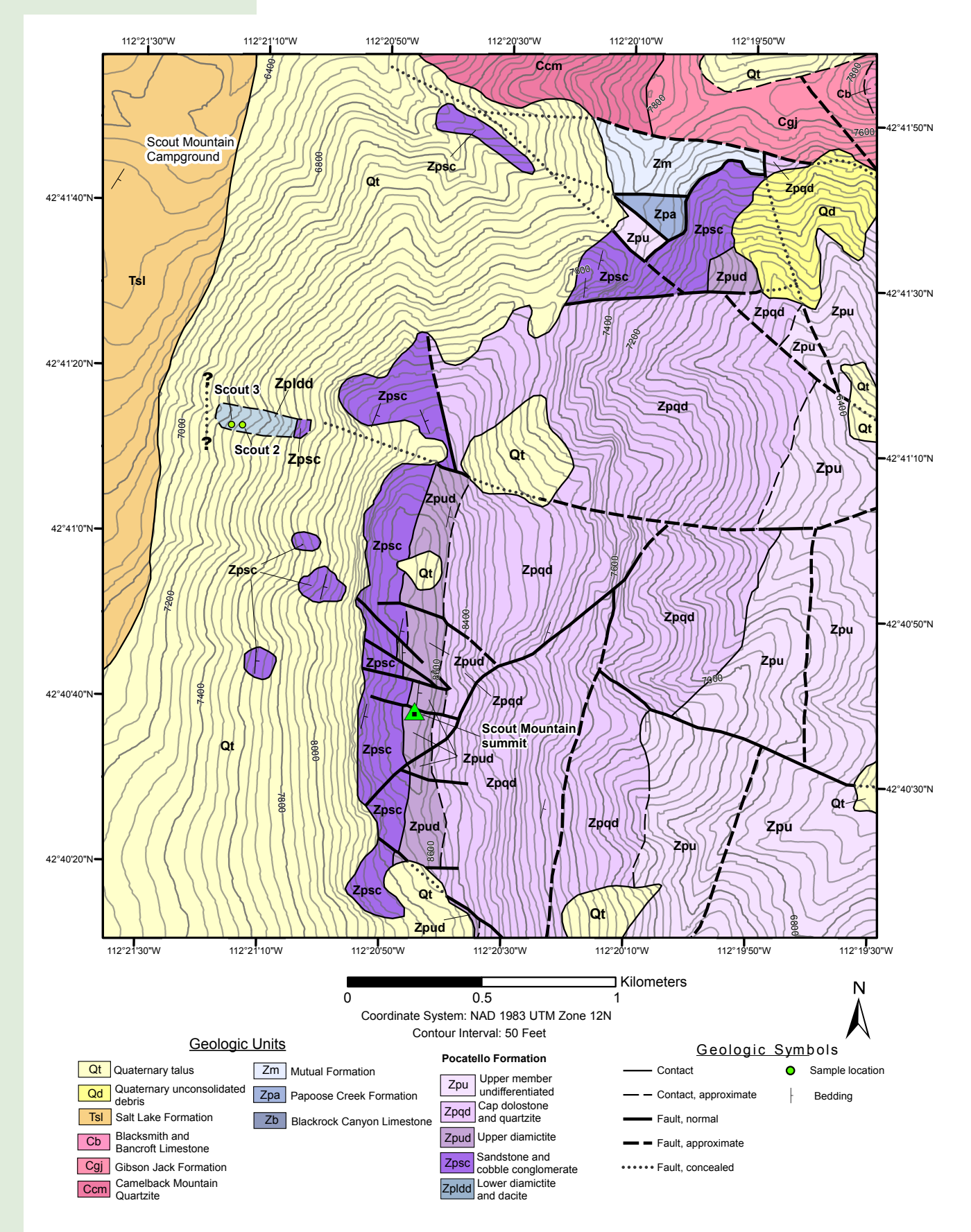


Figure 3. Geologic map of the northwestern side of Scout Mountain, southeastern Idaho, modified from Platt (1998), showing sample locations of this study (green circles). NAD 1983—North American Datum of 1983; UTM—Universal Transverse Mercator.

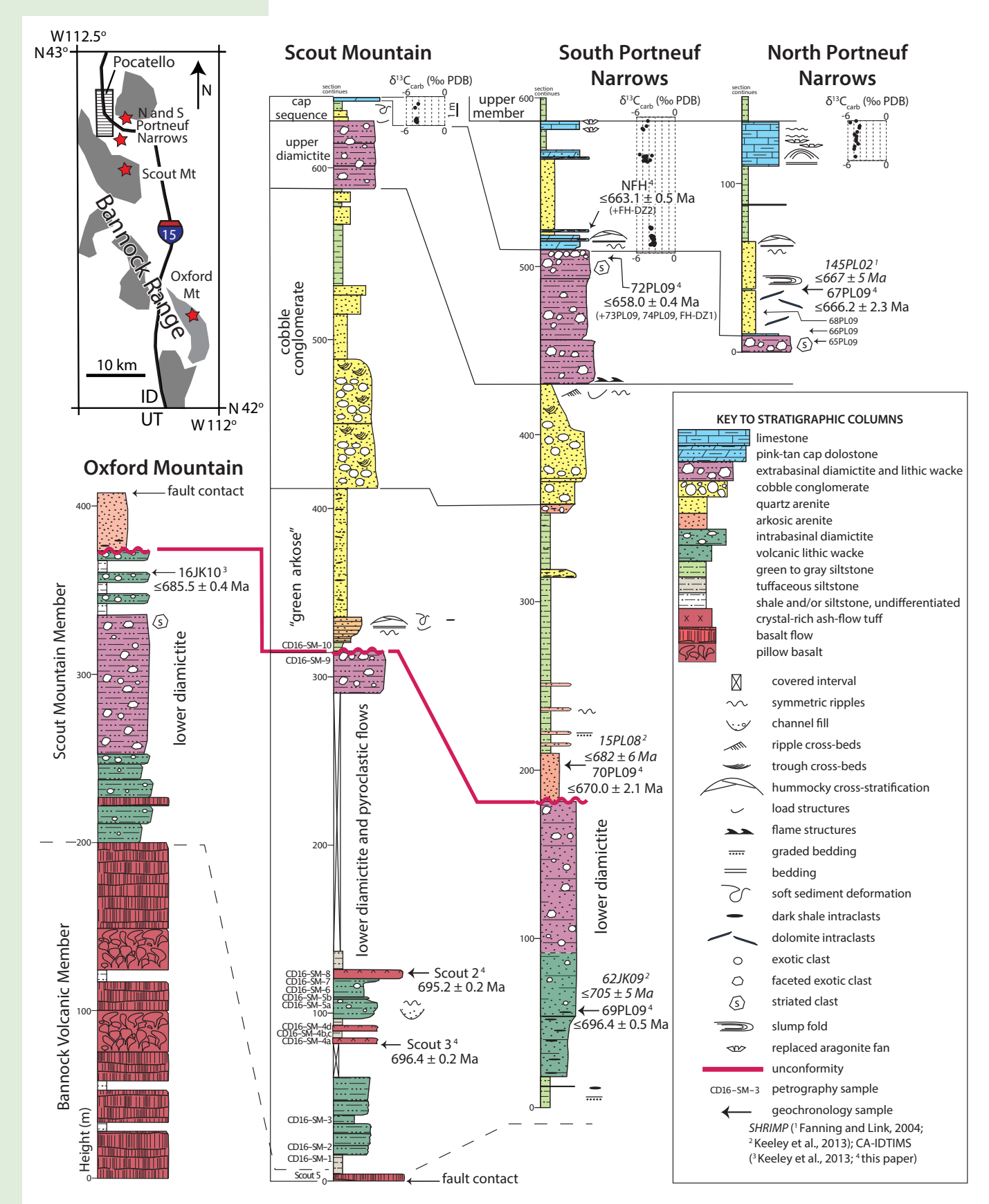


Figure 4. Stratigraphic sections for the Pocatello Formation exposed at Oxford Mountain (modified from Keeley et al., 2013), Portneuf Narrows (Dehler et al., 2011), and Scout Mountain (this study), Idaho, illustrating sedimentological characteristics, stratal geometry, unconformities, correlations, and the positions of dated detrital and volcanic horizons. Map inset: Gray shading indicates high topography of the Bannock Range; ID—Idaho; UT—Utah. δ¹³C_{carb} (% PDB) are measurements of the carbon isotope composition of limestone or dolostone, measured with respect to the Peedee belemnite standard.

The succession north of Portneuf Narrows is overturned; however, the top of the upper diamictite, the overlying meter-thick cap dolostone, and the rest of the Scout Mountain Member are clearly exposed. We collected samples of the upper diamictite (65PL09), overlying quartz arenite sandstone (66PL09) and siltstone (68PL09), and the "reworked fallout tuff" bed (67PL09) of Fanning and Link (2004) located ~20 m (stratigraphically) above the upper diamictite—cap dolostone contact.

Scout Mountain

Link (1982) described a section of Pocatello Formation strata including "dacite flows" on the western slope of Scout Mountain adjacent to an ephemeral stream draining into the Scout Mountain campground (Fig. 3). We measured and described this section (Fig. 4) from its base, where hydrothermally altered basaltic volcanic flows are in fault contact against indurated quartzite, possibly of the Brigham Group (Link, 1982), to the green arkosic sandstones unconformably overlying the lower diamictite (Fig. 5). Samples were collected for petrography, and thin-section photomicrographs for selected lithologies from this section are illustrated in the Supplemental Material and Figure 6. The entire section is characterized by a variably penetrative cleavage fabric of overprinting microcrystalline chlorite and/or biotite microlites and by a consistent superposed spaced cleavage of pressure-solution selvages. Cleavage is at a high angle to the primary bedding and does not obscure the primary volcanic and sedimentary depositional features of the deposits. Two dacitic crystal-lithic lapilli tuffs (samples Scout 2 and Scout 3) were sampled for U-Pb zircon geochronology from the transitional beds where the Bannock and Scout Mountain Members interfinger (Fig. 4).

METHODS

Zircon grains were separated from all samples (Table 1) using standard gravimetric and magnetic mineral separation techniques and placed in a muffle furnace at 900 °C for 60 h in quartz beakers to anneal minor radiation damage. Annealing (for both samples and standards) enhances cathodoluminescence (CL) emission (Nasdala et al., 2002), promotes more reproducible interelement fractionation during laser ablation–inductively coupled plasma mass spectrometry (LA-ICPMS) (Allen and Campbell, 2012), and prepares the crystals for subsequent chemical abrasion (Mattinson, 2005). Following annealing, both random and hand-picked aliquots of crystals were mounted, polished,

and imaged by CL on a JEOL T-300 scanning electron microscope fitted with a GATAN MiniCL detector at Boise State University (Boise, Idaho). CL images were used to identify internal zircon features and morphological traits for determining preferred spot locations for U-Pb and trace element LA-ICPMS using a New Wave Research UP213 Nd:YAG laser probe coupled to an X-Series 2 quadrupole mass spectrometer according to the methods described in Rivera at al. (2013). Zircon crystals were ablated with a laser diameter of 25 or 30 μm using laser fluence and pulse rates of 4 J/cm² and 5 Hz, respectively, during a 45 s analysis (15 s gas blank, 30 s ablation) that excavated a pit ~25 μm deep. Further details of the analytical method are collated in Table S1 of the Supplemental Material (footnote 1).

For U-Pb dates, instrumental fractionation of the background-subtracted ²⁰⁶Pb/²³⁸U and ²⁰⁷Pb/²⁰⁶Pb ratios was corrected and dates were calibrated with respect to interspersed measurements of the Plešovice zircon standard (Sláma et al., 2008). Signals at mass 204 were indistinguishable from zero following subtraction of mercury backgrounds measured during the gas blank (<120 cps ²⁰²Hg), and thus dates are reported without common Pb correction. Radiogenic isotope ratio and age error propagation for each spot includes uncertainty contributions from counting statistics and background subtraction as well as the propagated uncertainty of instrumental fractionation estimated from repeated measurements of the primary standard according to the reporting protocols recommended by Horstwood et al. (2016). For concentration calculations, background-subtracted count rates for each analyte were internally normalized to ²⁹Si and calibrated with respect to NIST SRM-612 and NIST SRM-610 glasses as the primary standards. Analytical results are summarized in Tables S2 and S3 of the Supplemental Material (footnote 1).

Following LA-ICPMS analyses, individual grains with concordant Cryogenian spot dates were plucked from the epoxy and chemically abraded following a procedure modified from Mattinson (2005). Sixteen (16) grains were fragmented prior to chemical abrasion in order to test the within-grain reproducibility of isotope ratios through the chemical abrasion process. Individual crystal fragments were subjected to a single high-temperature hydrofluoric acid treatment for 12 h to aggressively remove damaged regions that may have experienced Pb loss. The temperature of this chemical-abrasion step was varied from 180 °C to 200 °C between different experiments in order to mitigate variable Pb loss as a function of uranium concentration while maintaining a satisfactory volume of residual zircon for subsequent isotopedilution analysis. These residual crystals were spiked with an EARTHTIME mixed 205Pb-233U-235U tracer solution (ET535) and dissolved for 48 h at 220 °C. U and Pb were separated from solution via ion chromatography following Krogh (1973) and loaded onto a single rhenium filament in preparation for sequential U-Pb TIMS analysis using an IsotopX Isoprobe-T multi-collector TIMS fitted with an ion-counting Daly detector for single collector Pb isotope analysis and $10^{12} \Omega$ resistor amplifiers for static Faraday analysis of U isotopes.

Uranium-lead dates and uncertainties for each analysis were calculated using the algorithms of Schmitz and Schoene (2007) and the U decay constants of Jaffey et al. (1971). Other details of analytical parameters can be found in

Supplemental Material. Figure S1. Thin-section photomicrographs for lithologies of the Bannock Volcanic Member and Scout Mountain Member of the Pocatello Formation exposed at Scout Mountain, Idaho. Sample numbers are illustrated on the stratigraphic section of Figure 4. Field of view is 24 mm × 40 mm. Tables S1–S3: LA-ICPMS U-Pb isotope and trace element concentration data. Table S4: CA-IDTIMS U-Pb isotope data. Please visit https://doi.org/10.1130/GEOS.S.18335228 to access the supplemental material, and contact editing@geosociety.org with any questions.

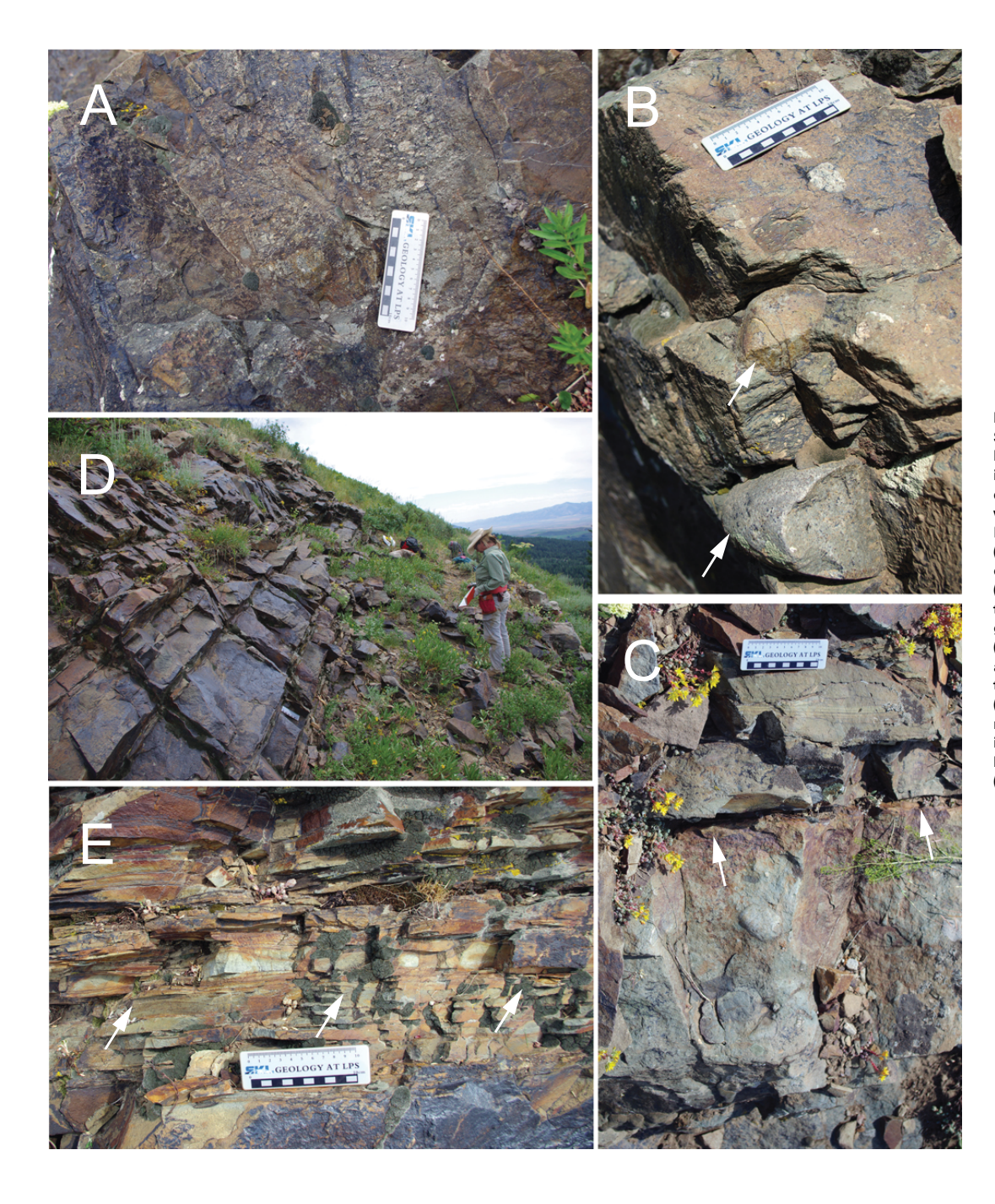


Figure 5. Outcrop photographs of the Scout Mountain Member of the Pocatello Formation. Scale shown in A, B, C, and E is in centimeters. (A) Heterogeneous pebblecobble diamictite interbedded with lithic wacke and dacitic pyroclastic flows (Scout Mountain). (B) Faceted quartzite cobbles (indicated by white arrows) near the top of the lower diamictite (Scout Mountain). (C) Sharp contact (at arrows) between the lower diamictite and the overlying green arkosic sandstone (Scout Mountain). (D) Tabular green arkosic sandstone beds above the lower diamictite (Scout Mountain). (E) Hummocky cross-stratification (HCS) within green arkosic sandstone (arrows are at the base of the HCS horizon), immediately above the contact with the lower diamictite unit (Scout Mountain). (Continued on following page.)

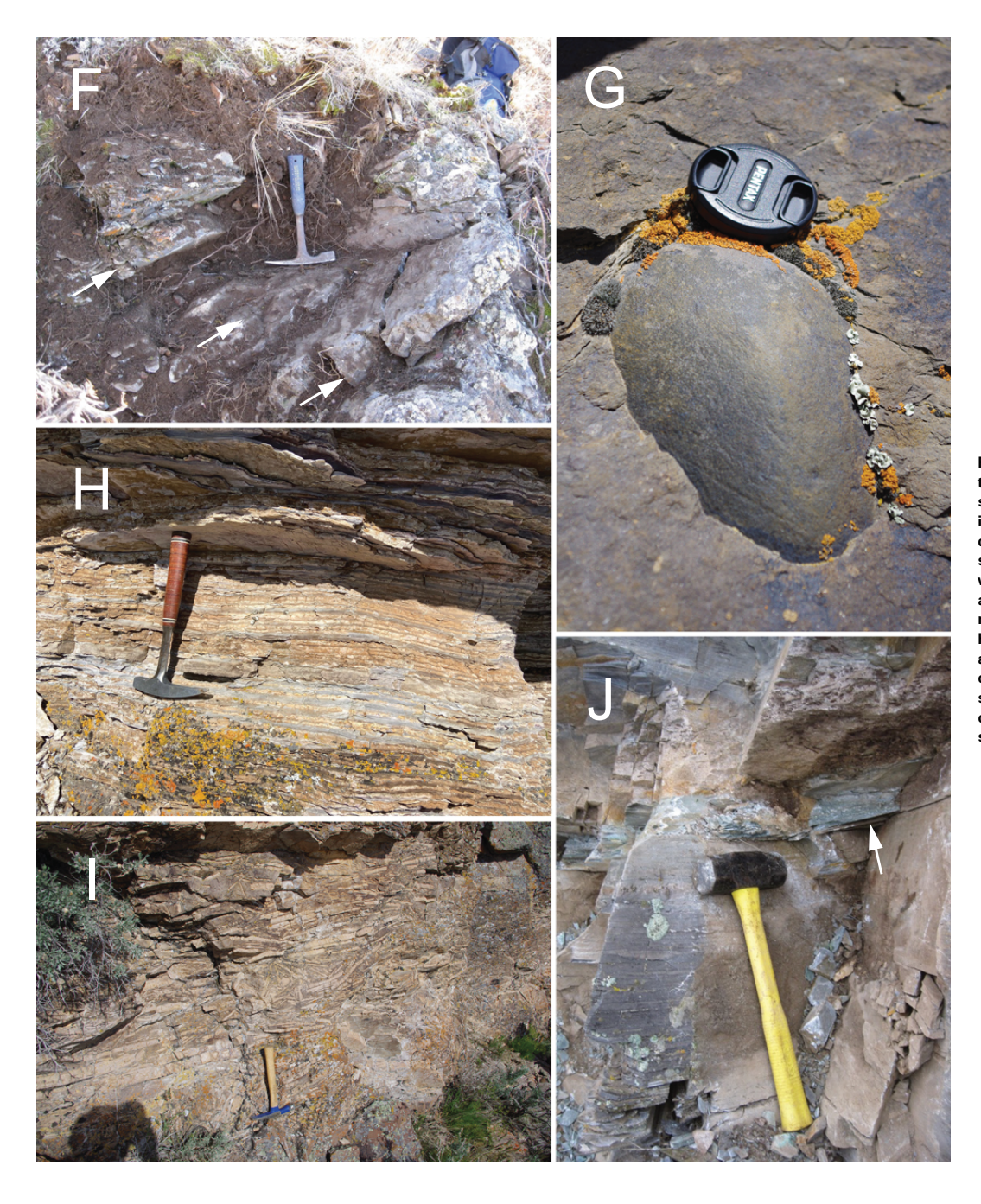


Figure 5 (continued). (F) Stratified diamictite at the top of the upper diamictite unit (Fort Hall section, south Portneuf Narrows). White arrows indicate strike of bedding. (G) Striated quartzite clast in upper diamictite unit (Fort Hall section, south Portneuf Narrows). (H) Cap dolostone with interbeds of mauve siltstone-sandstone above the upper diamictite (Fort Hall, south Portneuf Narrows). (I) Cap dolostone breccias (Fort Hall section, south Portneuf Narrows). (J) White arrow pointing to "reworked airfall tuff" horizon of Fanning and Link (2004), appearing as a green siltstone drape within the sandstone sequence overlying the upper diamictite—cap dolostone sequence (north Portneuf Narrows).

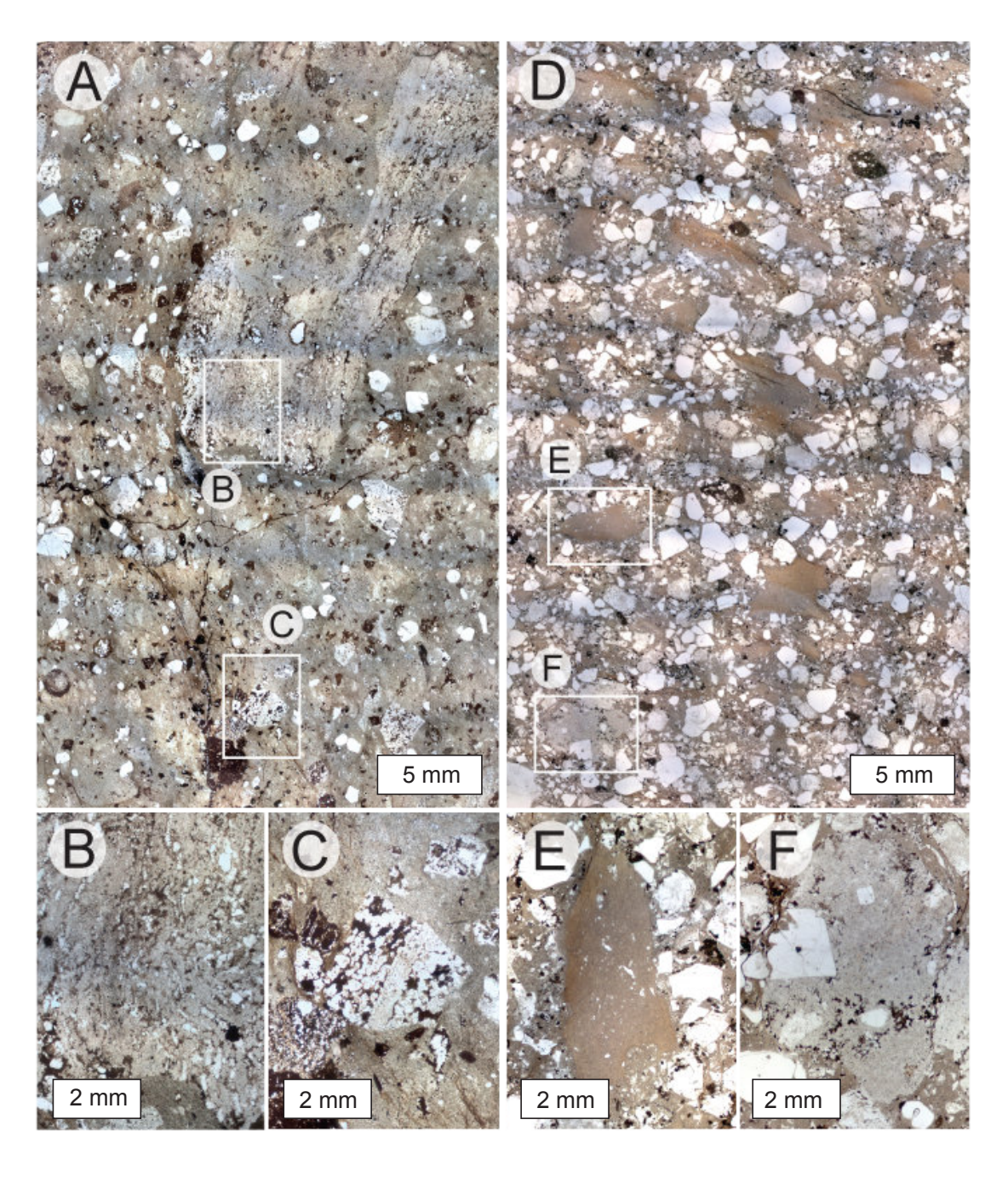


Figure 6. Thin-section photomicrographs (27 x 46 mm) for volcanic facies within the Scout Mountain Member of the Pocatello Formation at Scout Mountain. (A) Sample Scout 2: Dacitic ash-flow tuff with quartz phenocrysts and lapilli pyroclasts. (B) Folded flow banding in a pumiceous lapilli fragment. (C) Spherulitic-textured, banded lapilli fragment. (D) Sample Scout 3: Crystal-rich dacitic ash-flow tuff with quartz and feldspar phenocrysts and lapilli pyroclasts. (E) (rotated 90° clockwise) **Cuspate-margined pseudomorph after** glass lapilli pyroclast. (F) (rotated 90° clockwise) Holocrystalline quartz-bearing lapilli fragment.

TABLE 1. SAMPLES FROM THE SCOUT MOUNTAIN MEMBER, POCATELLO FORMATION, IDAHO, USA

Sample no.	Lithology	Location	UTM (NAD83)	Latitude (°N)	Longitude (°W)	Age constraint (Ma)
67PL09	Green siltstone	Portneuf Narrows North	12T 389421 4740230	42.80664	112.35241	≤666.2 ± 2.3
68PL09	Green siltstone	Portneuf Narrows North	12T 389430 4740250	42.80682	112.35231	≤664.1 ± 4.3
66PL09	Quartz arenite sandstone	Portneuf Narrows North	12T 389384 4740254	42.80685	112.35287	≤674.3 ± 0.5
NFH	Cap dolostone	Portneuf Narrows South	12T 389416 4736950	42.77711	112.35183	≤663.1 ± 0.5
FH-DZ2	Cap dolostone, sandy interbed	Portneuf Narrows South	12T 389427 4736831	42.77604	112.35168	≤663.9 ± 1.8
74PL09	Stratified diamictite (upper)	Portneuf Narrows South	12T 389427 4736831	42.77604	112.35168	N/A
73PL09	Stratified diamictite (upper)	Portneuf Narrows South	12T 389427 4736831	42.77604	112.35168	≤683.1 ± 0.5
FH-DZ1	Massive diamictite (upper)	Portneuf Narrows South	12T 389427 4736831	42.77604	112.35168	≤680.6 ± 0.5
72PL09	Massive diamictite (upper)	Portneuf Narrows South	12T 389427 4736831	42.77604	112.35168	≤658.0 ± 0.4
65PL09	Massive diamictite (upper)	Portneuf Narrows North	12T 389384 4740254	42.80685	112.35287	≤682.1 ± 0.9
70PL09	Arkosic arenite sandstone	Portneuf Narrows South	12T 389151 4737529	42.78228	112.35518	≤670.0 ± 2.1
69PL09	Diamictite (lower)	Portneuf Narrows South	12T 388787 4738331	42.78945	112.35979	≤696.4 ± 0.5
Scout 2	Dacitic crystal-lithic lapilli tuff	Scout Mountain	12T 389105 4726924	42.68681	112.35367	695.17 ± 0.20
Scout 3	Dacitic crystal-lithic lapilli tuff	Scout Mountain	12T 389057 4726934	42.68689	112.35425	696.43 ± 0.21

Note: Geographic information: UTM—Universal Transverse Mercator; NAD83—North American 1983 datum; UTM coordinates listed as Zone Easting Northing. Age constraints: Detrital zircon maximum depositional ages for sedimentary rocks are indicated by the ≤ symbol, with uncertainties defined by the youngest single grain analysis; igneous crystallization ages have uncertainties defined by the standard error of the weighted mean of multiple single crystal fragments (see text for details); N/A—not analyzed.

the notes to Table S4 of the Supplemental Material (footnote 1). Uncertainties are based upon non-systematic analytical errors, including counting statistics, instrumental fractionation, tracer subtraction, and blank subtraction. These error estimates should be considered when comparing our $^{206}\text{Pb}/^{238}\text{U}$ dates with those from other laboratories that used tracer solutions calibrated against the EARTHTIME gravimetric standards. When comparing our dates with those derived from other decay schemes (e.g., $^{40}\text{Ar}/^{39}\text{Ar}$, $^{187}\text{Re}^{-187}\text{Os}$), the uncertainties in tracer calibration (0.03%; Condon et al., 2015; McLean et al., 2015) and U decay constants (0.108%; Jaffey et al., 1971) should be added to the internal error in quadrature. Sample ages are thus reported as $\pm X(Y)[Z]$ Ma, where X is the internal error, Y is the internal plus tracer calibration error, and Z is the internal plus tracer plus decay constant uncertainty.

RESULTS

Stratigraphy of the Scout Mountain Member, Western Scout Mountain

From the base of the measured section on Scout Mountain (Fig. 4), the first unit comprises 4.5 m of hydrothermally altered and silicified volcanic flows with quartz-filled amygdules, interpreted as basaltic to basaltic andesite in composition based upon the plagioclase phenocrysts and groundmass composition. At least two flows are distinguished on the basis of vesicular flow tops. Overlying these effusive flows with apparent conformity is a >5-m-thick unit of whitish-weathering, silicified siltstone, tabular bedded on a decimeter scale; this unit is tentatively identified as a mixed holoclastic and basaltic

tuffaceous deposit. The next unit comprises ~55 m of poorly sorted, feldspathic lithic wacke containing abundant angular milky quartz and altered feldspar crystals, granules of quartzite and brown-weathering biotite aggregates, and fine-grained white holocrystalline lithic fragments with outsized quartz phenocrysts, all in a recrystallized micaceous matrix. Coarse sand to granule-rich beds of wacke alternate with clast-poor beds on a decimeter scale.

Above an intervening ~20 m covered interval is a ~12-m-thick guartz- and feldspar-phyric, dacitic crystal-lithic lapilli tuff with a crystal- and lapilli-rich base grading to a crystal-poor ash-rich top (Fig. 4). This unit was intensively sampled for petrography and geochronology (samples Scout 3, CD16-SM-4 series). A second 3-m-thick ash flow tuff deposit was recognized conformably overlying the first pyroclastic deposit and exhibits similar compositional grading. The ash-flow tuff interval is overlain by ~26 m of poorly sorted lithic wacke and pebble-clast diamictite. The diamictite matrix of siltstone with sparse sand-sized quartz grains is crudely stratified at the decimeter scale, with millimeter- to centimeter-thick mudstone lenses and trains of aligned clasts. Clast composition includes <2-3-cm-diameter subrounded mafic and angular white volcanic rocks, distinctive and ubiquitous black discoid micaceous clasts of similar size, and <10-cm-diameter subrounded quartzite (Fig. 5A). The entire unit coarsens upward in the lower 11 m before transitioning into a clast-poor, poorly sorted, fine-grained lithic wacke with dispersed coarse sand grains composed of quartz, feldspar, and angular white lithic fragments

Beds in the upper portion of this lithic wacke and diamictite unit have erosive bases creating 30–60-cm-deep relief in the tops of underlying beds, which are filled with lenticular bodies of pebble conglomerate. Angular 2–5-cm-diameter white volcanic clasts reappear in the lithic wacke in its upper 4 m.

Another 7 m interval of dacitic ash-flow tuff succeeds the lithic wacke and pebble diamictite. This pyroclastic deposit is characterized by a quartz- and plagioclase-phyric composition with abundant spherulitic and holocrystal-line lapilli fragments in a waxy green matrix. This interval was sampled for petrography and geochronology (samples CD16-SM-8, Scout 2). Another 10 m of buff-green siltstone with stranded fine lapilli fragments overlies the crystal-and lapilli-rich pyroclastics.

A thick covered interval with patchy subcrop of greenish medium-grained sandstone and gray coarse-grained sandstone transitions into abundant colluvial talus piles and intervening outcrops of matrix-supported pebble to cobble diamictite (Fig. 5B). The diamictite has a siltstone to fine-grained sandstone matrix that weathers to a rosy pink-gray surface and erodes into flaggy sheets. Subrounded to rounded clasts comprise quartzite (5–30 cm diameter), aphanitic greenstone (3–5 cm), granitoid (2–10 cm), and a variety of vesicular, porphyritic, and aphanitic basalts (2–15 cm).

A sharp, planar, erosive disconformity separates diamictite from overlying green arkosic sandstone at 309.5 m above the base of the section (Fig. 5C) This unit comprises ~10-cm-thick tabular packages of well-sorted, fine-grained feldspathic arenite sandstone grading upward through siltstone to mudstone drapes; beds thicken and coarsen upward and can be traced along strike for tens of meters (Fig. 5D). The bottoms of beds exhibit common load structures and tool marks. In between many of these decimeter-thick sandstone layers are thinly laminated, bedded packages of fine-grained sandstone and siltstone with symmetric ripples and hummocky cross-stratified (HCS) bedforms (Cheel and Leckie, 1993). The HCS bedforms are flat based, with low-amplitude, 20 cm wavelengths, and contain truncated very low-angle and parallel lamination (Fig. 5E). Such bedforms were likely generated below fair-weather wave base and subject to open-water fetch and storm-wave action. Although we did not measure a new section above this arkosic sandstone interval, we augment our measured section with that of Link (1982, their plate 4, section 13). These HCS beds are succeeded by ~75 m of thick-bedded quartz arenite followed by an additional ~75 m of clast-supported cobble conglomerate. This conglomerate contains granitic, gneissic, quartzitic, and felsic volcanic clasts and exhibits internal channels and trough cross-bedding characteristic of a braided fluvial environment. The cobble conglomerate is succeeded by an additional ~43 m of sandstone and ~57 m of thin-bedded siltstone and sandstone, interpreted to represent a return to a marine environment. This sequence is sharply overlain by ~40 m of weakly stratified matrix-supported "upper" diamictite with an overlying cap dolostone poorly exposed at the top of the Scout Mountain section (Fig. 4).

Stratigraphy of the Upper Diamictite—Cap Dolostone Transition (Scout Mountain Member) at Portneuf Narrows

The contact between the upper diamictite and overlying cap dolostone interval in the Portneuf Narrows area is typically covered, but it has been

excavated in several places south of Portneuf Narrows and is traceable across the southern Portneuf Narrows ridge. In the Fort Hall area, the top of the diamictite contains crudely stratified pebble- to boulder-sized clast diamictite, which is sharply overlain by thin-bedded sandstone with granule- to silt-sized grains and ripple cross-lamination. This 40 cm interval is the color of the diamictite matrix and commonly has a calcareous cement.

Above this interval (although the lower 4 m is typically covered) is 17 m of thin-bedded dolostone interbedded with thin, rippled beds of fine-grained micaceous sandstone, dolomite-chip breccia, and sandstone with HCS bedforms, parting lineations, and soft-sediment deformation (unit A of Dehler et al., 2011). This cap dolostone sequence is consistent with deposition during glacio-eustatic transgression and, although it is a sharp contact, does not necessitate significant erosion between the diamictite and the cap dolostone (cf. Kennedy, 1996). This interval is very similar to siliciclastic-rich Marinoan diamictite-cap dolostone intervals worldwide (Hoffman et al., 2011), supporting a genetic relationship between the upper diamictite and the overlying cap dolostone in the Pocatello Formation.

U-Pb Zircon Geochronology: Volcanic Rocks

Thin-section petrography of the Scout 2 and Scout 3 samples of dacitic crystal-lithic lapilli tuff provides several observations bearing on their pyroclastic volcanic origins (Fig. 6). Sample Scout 2 contains 2–20-mm-diameter folded flow banded and/or spherulitic pumiceous lapilli fragments, bipyramidal and fractured quartz, saussuritized plagioclase, and tabular opaque oxide phenocrysts in a fine matrix interpreted to have been deposited as volcanic ash (Figs. 6A–6C). Sample Scout 3 contains 3–5-mm-diameter cuspate-margined fine-grained ash lapilli pyroclasts as well as holocrystalline quartz-bearing lapilli fragments in a crystal-rich fine ash matrix (Figs. 6D–6F). Phenocrysts include abundant bipyramidal and fractured quartz and subordinate tabular saussuritized plagioclase crystals. Furthermore, the zircon crystals separated from both samples display uniform morphology and CL response and lack any evidence of abrasion or rounding.

The LA-ICPMS results from the dacitic crystal-lithic lapilli tuffs (samples Scout 2 and Scout 3) yield unimodal normal distributions of Neoproterozoic U-Pb dates ranging from 777 \pm 54 to 610 \pm 20 Ma, with weighted means of 665 \pm 16 and 655 \pm 11 Ma, respectively. Initial IDTIMS analyses on a set of grains from both samples without chemical-abrasion pretreatment yielded scattered and discordant U-Pb dates (ca. 690–624 Ma) defining Pb-loss arrays (Fig. 7). Chemical abrasion at 180 °C yielded a narrower spread of more concordant, older U-Pb dates ranging from ca. 703 to 695 Ma, while a third round of CA-IDTIMS analysis using more aggressive chemical abrasion at 200 °C also yielded the same narrow range. Chemically abraded zircon samples from both tuffs exhibit a similar pattern, with a majority of analyses defining a cluster of younger dates and a minority of analyses spreading to older dates (Fig. 7). The youngest mode of dates for each sample yield weighted mean U-Pb dates of 696.43 \pm 0.21(0.39)

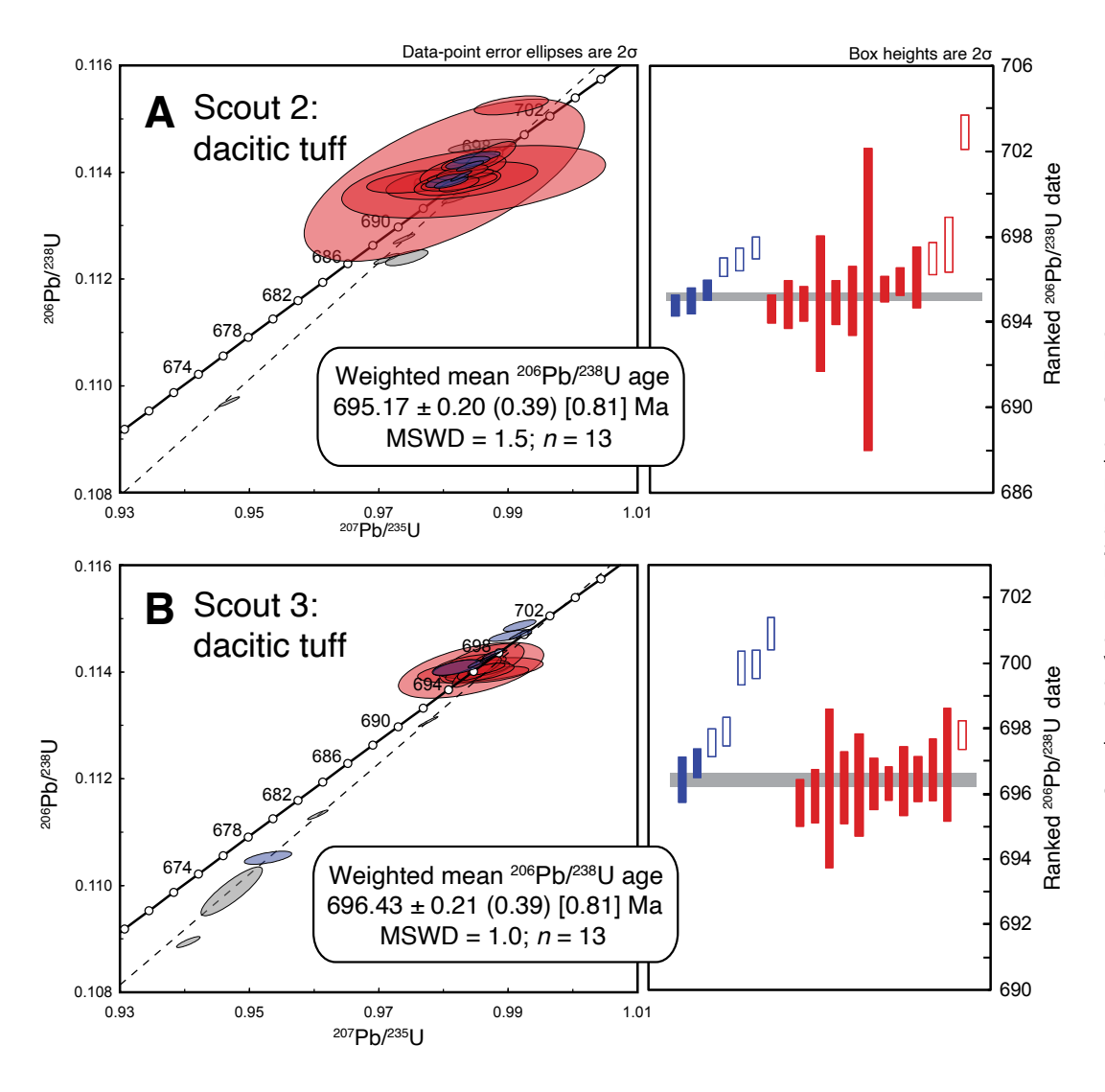


Figure 7. U-Pb Wetherill concordia diagrams and ranked 206Pb/238U weighted mean plots of CA-IDTIMS data for samples Scout 2 (A) and Scout 3 (B) dacitic crystal-lithic lapilli tuffs from Scout Mountain. Gray ellipses represent analyses without chemical abrasion that define linear arrays reflecting Pb loss. Blue error ellipses and bars represent analyses using 180 °C chemical abrasion, and red error symbols using 200 °C chemical abrasion. Solid bars represent data used in the weighted mean age calculation. Horizontal gray bar represents the weighted mean age and uncertainty (95% confidence interval). Weighted mean ages are reported as $\pm X(Y)[Z]$ Ma, where X is the internal error, Y is the internal plus tracer calibration error, and Z is the internal plus tracer plus decay constant uncertainty. MSWD is the mean squared weighted deviation of Wendt and Carl (1991).

[0.81] Ma (sample Scout 3; n=13 of 21; mean squared weighted deviation (MSWD) = 1.0) and $695.17 \pm 0.20(0.39)[0.81]$ Ma (sample Scout 2; n=13 of 19; MSWD = 1.5), in accord with stratigraphic superposition and thus interpreted to represent the timing of magmatic evolution culminating in eruption of each tuff. We attribute the minor spread to older dates to antecrystic inheritance that may have occurred during source partial melting, pre-eruptive upper-crustal storage, or climactic eruption (Rivera et al., 2013; Michel et al., 2016).

U-Pb Zircon Geochronology: Sedimentary Rocks

Laser ablation–inductively coupled plasma mass spectrometry (LA-ICPMS) analyses for the lower diamictite sample (69PL09, equivalent to sample 62JK09 of Keeley et al., 2013) yield a range of U-Pb dates between ca. 625 and 760 Ma with a dominant mode at ca. 700 Ma, and a few scattered dates from ca. 1670 to 1120 Ma (Fig. 8). CA-IDTIMS analyses on 25 grains selected from the

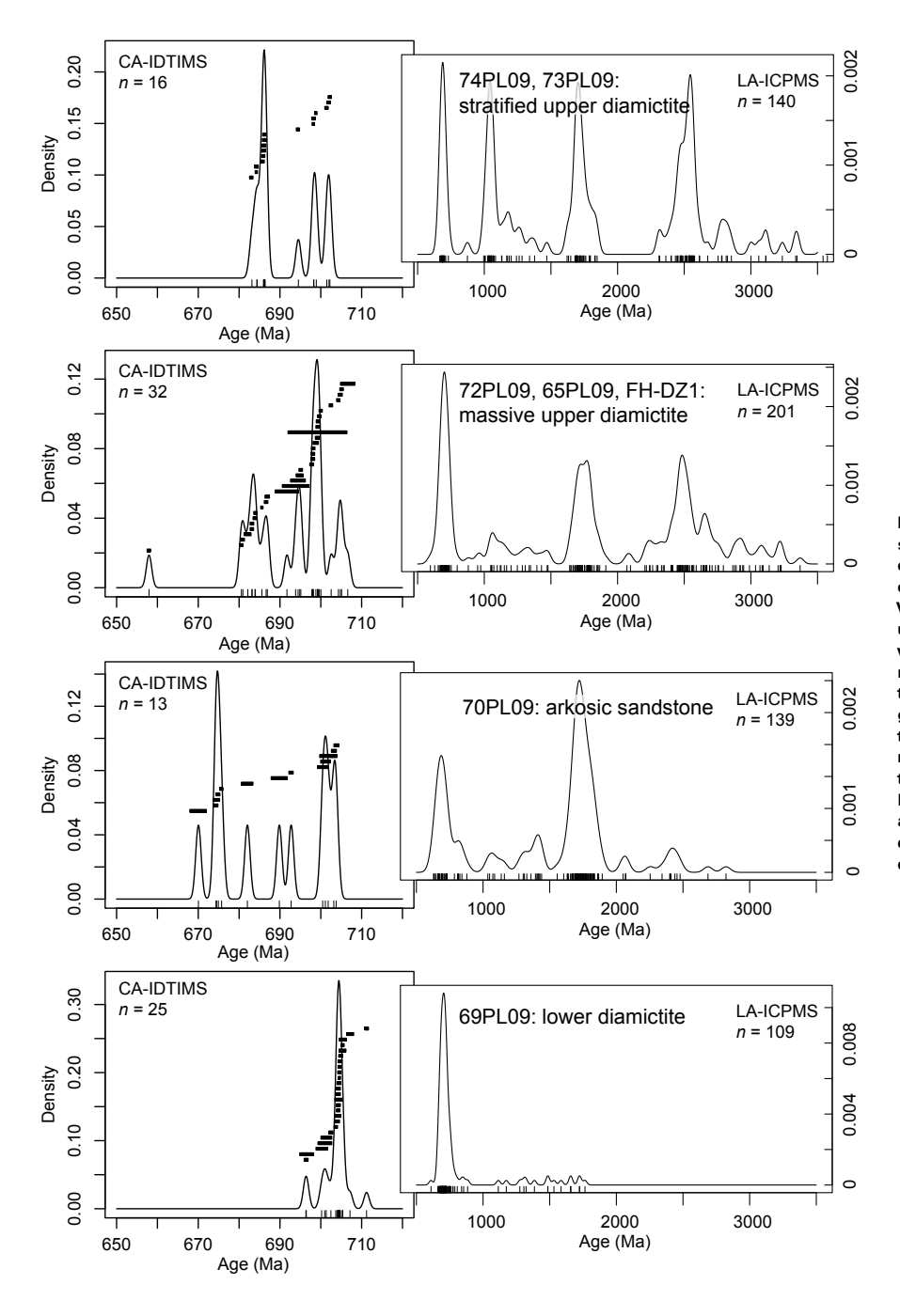


Figure 8. Kernel density estimates (KDEs) for samples of the Scout Mountain Member (Pocatello Formation) at Portneuf Narrows, Idaho, calculated using the "provenance" package of Vermeesch et al. (2016). Panels on the right document the KDEs for the entire sample aliquot via laser ablation-inductively coupled plasma mass spectrometry (LA-ICPMS) analyses, and the panels on the left define the KDEs for Cryogenian zircons via CA-IDTIMS analyses from the same samples, including superimposed ranked ²⁰⁶Pb/²³⁸U dates (plotted at 2σ). KDEs for the CA-IDTIMS results were calculated with a bandwidth of 0.665 optimized from all pooled analyses. Vertical ticks along the horizontal axes denote the mean values of each analyzed zircon crystal. (Continued on following page.)

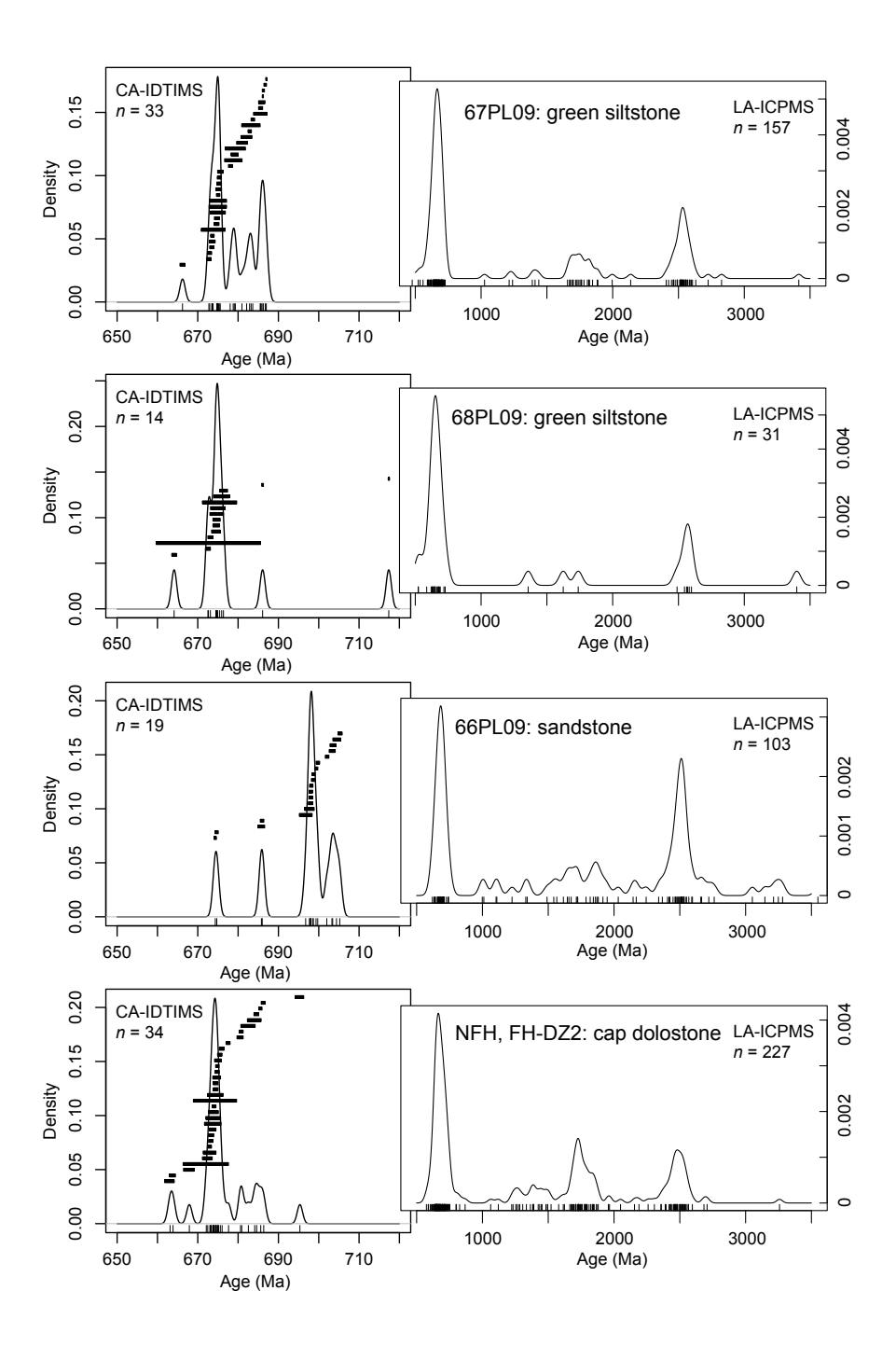


Figure 8 (continued).

e/article-pdf/18/2/825/5575955/825.pdf

youngest apparent LA-ICPMS dates yield single-grain U-Pb dates ranging from ca. 711.2 Ma to 696.4 Ma with a dominant mode at 704.5 Ma.

The arkosic sandstone resting unconformably above the lower diamictite (sample 70PL09, equivalent to sample 15PL08 of Keeley et al., 2013) yields two dominant modes of LA-ICPMS U-Pb dates at 1720 and 700 Ma along with a few scattered dates between the modes and as old as ca. 2830 Ma (Fig. 8). CA-IDTIMS analyses on 13 grains with the youngest LA-ICPMS spot dates yield a range of U-Pb dates from 703.8 Ma to 670.0 Ma with a youngest dominant mode at 674.9 Ma.

We pooled analyses of three samples of matrix from non-stratified upper diamictite (72PL09, 65PL09, FH-DZ1) collected near its top, one from the north side of Portneuf Narrows and two within a restricted stratigraphic interval from the Fort Hall section on the south side of Portneuf Narrows (Fig. 4). The LA-ICPMS U-Pb kernel density estimate of the pooled sample exhibits modes at 2500, 1750, and 700 Ma, with dates as old as 3350 Ma (Fig. 8). CA-IDTIMS analyses on 32 grains with Neoproterozoic LA-ICPMS spot dates yield a range of U-Pb dates from 706.6 to 657.9 Ma with many modes including at ca. 705, 700, 695, and 685 Ma. The youngest grain at 657.9 ± 0.2 Ma provides a maximum depositional age for the upper diamictite unit.

Two samples of stratified upper diamictite (73PL09, 74PL09) in the upper 20 cm of its exposure in the Fort Hall section have similar detrital provenance modes to the non-stratified upper diamictite, with the additional emergence of a 1160 Ma mode (Fig. 8). CA-IDTIMS analyses on 16 grains with the youngest LA-ICPMS spot dates yield a range of U-Pb dates from 702.2 to 683.1 Ma, again with similar modes in the CA-IDTIMS spectra compared to the non-stratified upper diamictite.

A sample of cap dolostone in the North Fort Hall section (sample NFH) and a sandy interbed within the cap dolostone in the Fort Hall section (sample FH-DZ2) on the south side of Portneuf Narrows pooled together yield a LA-ICPMS U-Pb kernel density estimate with a return to modes at 2500, 1750, and 700 Ma (Fig. 8). CA-IDTIMS analyses on 34 crystals with Neoproterozoic LA-ICPMS spot dates yield a range of U-Pb dates from 695.3 to 663.1 Ma, with a kernal density estimate dominated by a strong mode at 674 Ma. A single grain yields the only anomalously young Ediacaran (613 Ma) date in our data set. We hypothesize that carbonate rocks like sample NFH might be particularly sensitive to incorporation of post-depositional detrital grains during younger karstification, clastic infiltration, and/or recrystallization. Another possibility is contamination during sampling of this dolostone, perhaps within unrecognized pedogenic carbonate rinds. We note that sample NFH is the only predominantly carbonate sample in this data set that might be affected by these phenomena. Exempting this analysis from further consideration, two young grains are reproducible at 663.5 ± 0.5 Ma and provide a more probable maximum depositional age for the cap dolostone unit.

Three siliciclastic beds collected above the upper diamictite and cap dolostone interval on the north side of Portneuf Narrows yield similar detrital zircon age spectra. One of these samples (67PL09) was extracted from the same event bed sampled by Fanning and Link (2004) that they described as a "reworked

fallout tuff". The zircon crystals extracted from these samples ranged from euhedral and prismatic (~60% of the population) to subrounded to rounded in morphology (~40% of the population). This heterogeneity in morphology is mimicked by the variability in LA-ICPMS spot dates that demonstrate mixed Neoproterozoic, Mesoproterozoic, and Archean sources (Fig. 8). This correlation of grain rounding and age is anticipated for multi-cycle, transported detrital zircons. These samples from sandstone and siltstone beds display a distinct detrital zircon provenance in the sediments above the cap dolostone in that the 2.5 Ga mode is dominant over the 1.7 Ga mode. CA-IDTIMS analysis on 19 Neoproterozoic grains selected from the lowest sandstone bed (sample 66PL09) yields U-Pb dates ranging from 705.2 to 674.3 Ma with the greatest mode at 699 Ma. The CA-IDTIMS kernel density estimates for the overlying green siltstones (samples 68PL09 and 67PL09), including the purported "reworked fallout tuff" sample, are similarly multi-modal, sharing a strong mode at 675 Ma, with grains as young as 666.2 and 664.1 Ma providing maximum depositional ages for these sedimentary rock samples containing abundant epiclastic volcanic detrital zircons.

DISCUSSION

Volcanic Beds Constraining the Sturtian-Aged "Lower Diamictite"

Laser ablation–inductively coupled plasma mass spectrometry (LA-ICPMS) analysis on zircons from the two dacitic tuffs in the Scout Mountain Member of the Pocatello Formation show normally distributed grain dates with weighted means of 665 ± 16 Ma (MSWD = 1.7, n = 11) and 655 ± 11 Ma (MSWD = 2.9, n = 28) from $\leq 10\%$ discordant analyses. Without adequate recognition of Pb loss in most of these zircon grains, it could be reasonably concluded from these LA-ICPMS dates that the entire Scout Mountain Member above the dacitic event beds was deposited post–Sturtian glaciation. However, our CA-IDTIMS data demonstrate the erroneous nature of this interpretation and highlight how the resolution of in situ techniques cannot detect and mitigate the effects of Pb loss, inheritance, or mixed epiclastic zircon ages.

CA-IDTIMS analysis utilizing differing levels of pretreatment chemical abrasion temperatures definitively identified and demonstrably reduced the amount of age discordance in zircon grains from these samples by eliminating zones of high uranium content, accumulated radiation damage, and variable Pb loss (Fig. 7) to produce precise and stratigraphically consistent (in sequence) dates of 696.4 ± 0.2 Ma and 695.2 ± 0.2 Ma. This study's tandem approach of dating using both LA-ICPMS and CA-IDTIMS on the same grains highlights the ubiquity of Pb loss in untreated zircon crystals and cautions against detailed age interpretation or correlation strictly from in situ techniques. On the other hand, independent CA-IDTIMS experiments yield reproducible results, with elevated chemical abrasion temperatures of 200 °C (note that increasing the temperature of chemical abrasion from 180 °C to 200 °C increases the dissolution rates by a factor of four) affirming that the original 180 °C results effectively

removed Pb-loss domains. These results illustrate the flexibility of the chemical abrasion methodology and the ability of repeated experimentation to establish confidence in the mitigation of Pb loss. We interpret these CA-IDTIMS dates on the basis of field and petrographic relationships as eruption and depositional ages for the two volcanic ash beds. These dated event beds thus provide robust syn-depositional age constraints for the lower diamictite in the Scout Mountain Member of the Pocatello Formation and tie these mixed volcanic and glacigenic strata to the 717–661 Ma Sturtian glaciation.

Following the same tandem LA-ICPMS and aggressive CA-IDTIMS procedure, our sample of the lower diamictite unit (69PL09) yields a youngest CA-IDTIMS U-Pb detrital zircon date of ca. 696.4 Ma. This youngest CA-IDTIMS date is indistinguishable from that of the underlying dacitic crystal-lithic lapilli tuffs, demonstrating local reworking of these volcanic units into penecontemporaneous and younger lower diamictite deposits in addition to epiclastic zircon crystals from volcanic rocks erupted over a 15 m.y. interval prior to deposition. The 696.4 and 695.2 Ma dacitic crystal-lithic lapilli tuff ages from Scout Mountain, when combined with the maximum depositional age constraint of 685.5 ± 0.4 Ma (Keeley et al., 2013) within the lower diamictite of the Oxford Mountain tuffite (Fig. 4), demand that the lower diamictite was deposited over at least 10 m.y. However, the dates of Keeley et al. (2013) remain interpretable only as maximum depositional ages, thus the upper portions of the lower diamictite unit may be younger. Similarly, the ~70 m of polymict lithic wacke below the dated pyroclastic flows represents an additional unknown duration of early Sturtian sedimentation.

Detrital Zircons Pointing to the Cryogenian Nonglacial Interval

The lower diamictite unit of the lower Scout Mountain Member exhibits an erosive top and a sharp discordance with an overlying arkosic sandstone (sample 70PL09) exhibiting graded bedding and hummocky cross-stratification. Sedimentary structures in the arkosic sandstone demonstrate its deposition below fair-weather wave base and subject to open-water fetch and storm-wave action, consistent with the interpretation that these units were deposited in non-glacial open water, rather than below an ice shelf, during the "Cryogenian nonglacial interval" (Halverson et al., 2020) between the Sturtian and Marinoan glaciations.

We interpret the cluster of ca. 675 Ma CA-IDTIMS dates in this arkosic sandstone to represent a robust maximum depositional age for the sandstone unit, and the single youngest 670 Ma zircon to further refine its age of deposition. An unconformity at the top of the lower diamictite is furthermore consistent with erosive removal of a Sturtian cap carbonate and diamictite at the studied locales of the Pocatello Formation. As such, it is possible if not probable that the >400 m of non-glacial siltstone, sandstone, and cobble conglomerate strata between the lower and upper diamictite units were deposited following Sturtian deglaciation at ca. 660 Ma (Zhou et al., 2019; Rooney et al., 2020).

An Abundance of Epiclastic Detrital Zircons and the Case for a Marinoan "Upper Diamictite"

Our sample (67PL09) of the "reworked fallout tuff bed" of Fanning and Link (2004) above the upper diamictite and cap dolostone at Portneuf Narrows yields a heterogeneous zircon population and multi-modal spread of LA-ICPMS and CA-IDTIMS dates more indicative of a detrital signal rather than volcanic fallout deposition (Fig. 8). CA-IDTIMS analyses on grains from the youngest mode yield a spread of dates ranging from 687 to 666 Ma, in stark contrast to the unimodal distribution of a volcanic event bed such as illustrated by the Scout 2 and Scout 3 tuff beds. This point is reinforced by the fact that the predominant (Cryogenian) mode of 675-673 Ma zircon grains in this bed are also found in underlying strata of the Scout Mountain Member, including both sampled clastic beds above the upper cap dolostone, the cap dolostone itself, and the arkosic sandstone sampled >400 m lower in the section, just above the lower diamictite (Figs. 4, 9). We conclude that a pyroclastic origin for this bed is untenable, and rather that it represents a siltstone with abundant locally sourced Cryogenian epiclastic volcanic detritus. In this conclusion, we echo the original interpretation of Fanning and Link (2004, p. 883), who wrote of their results: "As with all detrital zircons, this provides only a maximum age for the bed in question..." It is only in subsequent publications that a depositional age for this bed was entrenched in the literature (Link et al., 2005; Corsetti et al., 2007; Link and Christie-Blick, 2011).

The definitive removal of a minimum age constraint for the Scout Mountain Member leaves the timing of deposition of the upper glacial strata in the region open to new interpretation, given that the depositional age for the upper diamictite (and associated cap dolostone) is likely significantly younger than the ca. 670-675 Ma detrital zircons found in the upper Scout Mountain Member of the Pocatello Formation. The erosive unconformity and profound shift in sedimentology and detrital zircon provenance at the base of the arkosic sandstone overlying the lower diamictite and the subsequent deposition of ~300 m of non-glacial sedimentary strata have been highlighted earlier in this paper as the likely record of local erosion following the Sturtian deglaciation and subsequent marine deposition of the Cryogenian non-glacial interval. Sparse detrital zircon grains found in the upper diamictite and overlying cap dolostone with ages of 668, 664, 663, and 658 Ma (Fig. 9) further support a post-Sturtian deglaciation depositional history for the upper Scout Mountain Member and, by inference, a Marinoan identity for the upper diamictite and cap dolostone of the Pocatello Formation (e.g., Dehler et al., 2011; Petterson et al., 2011; Macdonald et al., 2013a). If correct, this age model reconciles the distinctive lithofacies, paleoenvironmental, and isotopic similarities of the cap dolostone in the upper Scout Mountain Member with other Marinoan cap dolostones worldwide. Further evidence for this two-glaciation hypothesis can and should be sought through additional high-resolution sedimentological and detrital zircon studies, particularly in the Scout Mountain section.

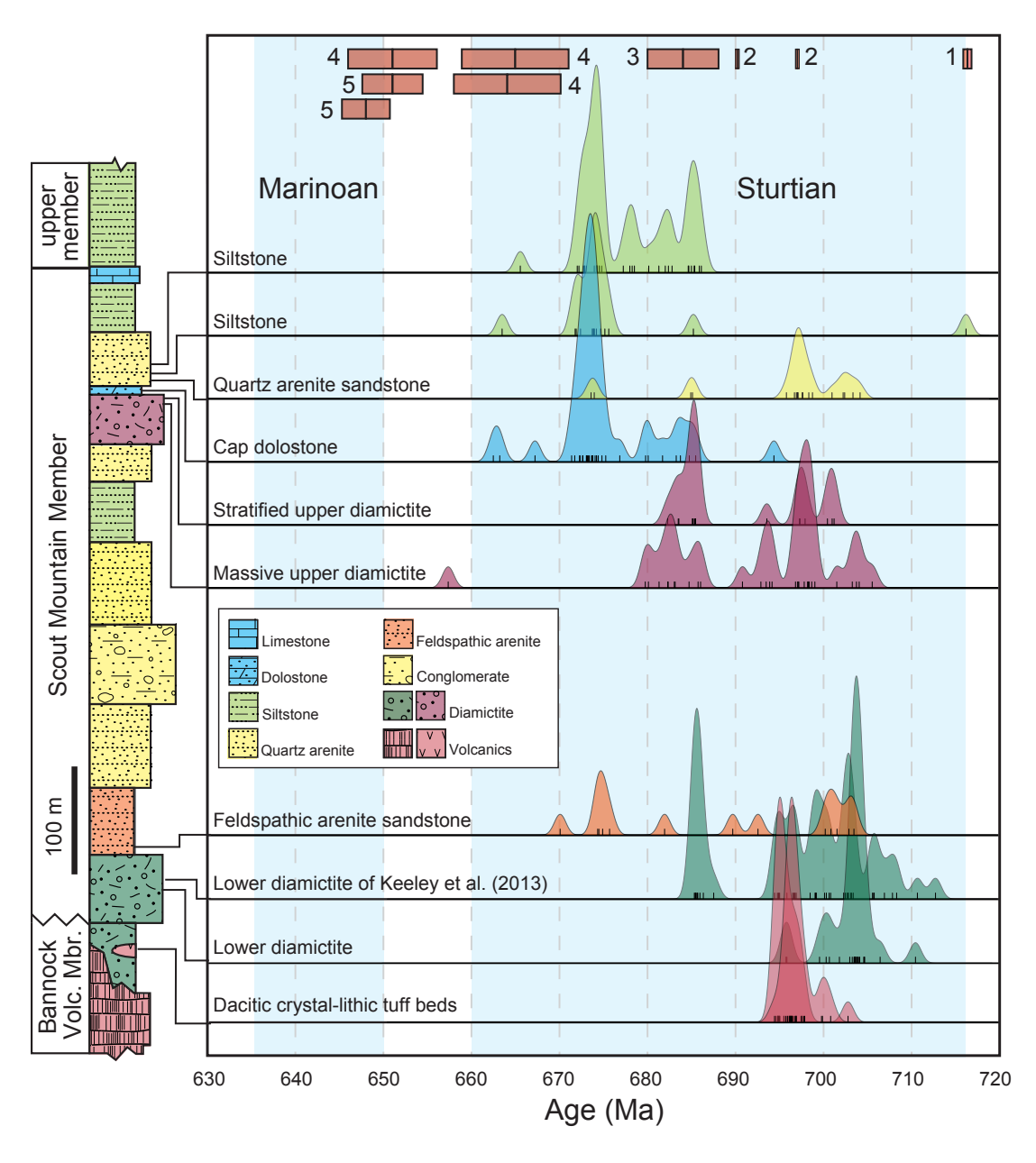


Figure 9. Compilation diagram of CA-IDTIMS ²⁰⁶Pb/²³⁸U kernel density estimates with stratigraphic context. At top for comparison are summarized selected Laurentian Cryogenian igneous volcanic and plutonic ages and errors (20): 1—Yukon, Canada (Macdonald et al., 2010); 2—northern British Columbia, Canada (Eyster et al., 2018); 3—central Idaho, USA (Lund et al., 2011); 5—southeastern Yukon (Pigage and Mortensen, 2004). Volc. Mbr.—Volcanic Member.

Pan-Laurentian Correlation of Two Cryogenian Glaciations

Traditional correlation of Neoproterozoic rocks along the North American Cordillera generally recognizes two phases of Cryogenian glaciation, represented by glacial deposits correlated with an older Sturtian glaciation and a younger Marinoan glaciation (e.g., Eisbacher, 1985). Complete sections of Sturtian and/or Marinoan glaciation-related deposits are unlikely due to erosional and structural omissions, and lithostratigraphic correlations are further complicated by syn-sedimentary tectonism associated with the protracted break-up of Rodinia (e.g., Li et al., 2008; Macdonald et al., 2013a). The Cryogenian stratigraphy of the northern Canadian Cordillera is probably the most well characterized due to extensive exposure and robust U-Pb zircon dates of 717.4 ± 0.2 and 716.9 ± 0.4 Ma (CA-IDTIMS) bracketing the onset of glacial sedimentation in the Rapitan Group (Macdonald et al., 2010, 2018) and a Re-Os date of 662.4 ± 3.9 Ma in the overlying cap limestone defining the termination of the Sturtian glaciation (Rooney et al., 2014, 2015) (Fig. 10). Additionally, a Re-Os depositional age of 632.3 ± 5.9 Ma was obtained on black shale in the basal Sheepbed Formation in the Mackenzie Mountains in the transgressive

sequence directly above the glacial deposits in the Stelfox Member of the Ice Brook Formation and the Ravensthroat cap dolostone (Rooney et al., 2015). This age agrees well with geochronological constraints on the termination of the Marinoan glaciation globally (e.g., Hoffmann et al., 2004; Condon et al., 2005; Calver et al., 2013; Prave et al., 2016).

Using the two-glaciation model for cross-Cordilleran correlations, the Sturtian Rapitan Group and the overlying ca. 662 Ma basal Twitya cap dolostone have been correlated with the Surprise Member diamictite and Sourdough Limestone of the Kingston Peak Formation in the Death Valley area, and the Marinoan Stelfox diamictite and Ravensthroat cap dolostone with the Wildrose diamictite and the Sentinel Peak Member of the Noonday Dolomite (e.g., Prave, 1999; Petterson et al., 2011; Macdonald et al., 2013a), an interpretation recently affirmed by the U-Pb zircon geochronology of Nelson et al. (2020). The strong chemo- and litho-stratigraphic similarities between the cap dolostone above the upper diamictite in Idaho and the Sentinel Peak Member in Death Valley support the hypothesis that the two glacigenic intervals in the Pocatello Formation also represent the Sturtian and Marinoan glaciations (Dehler et al., 2011; Petterson et al., 2011; Macdonald et al., 2013a). The data presented

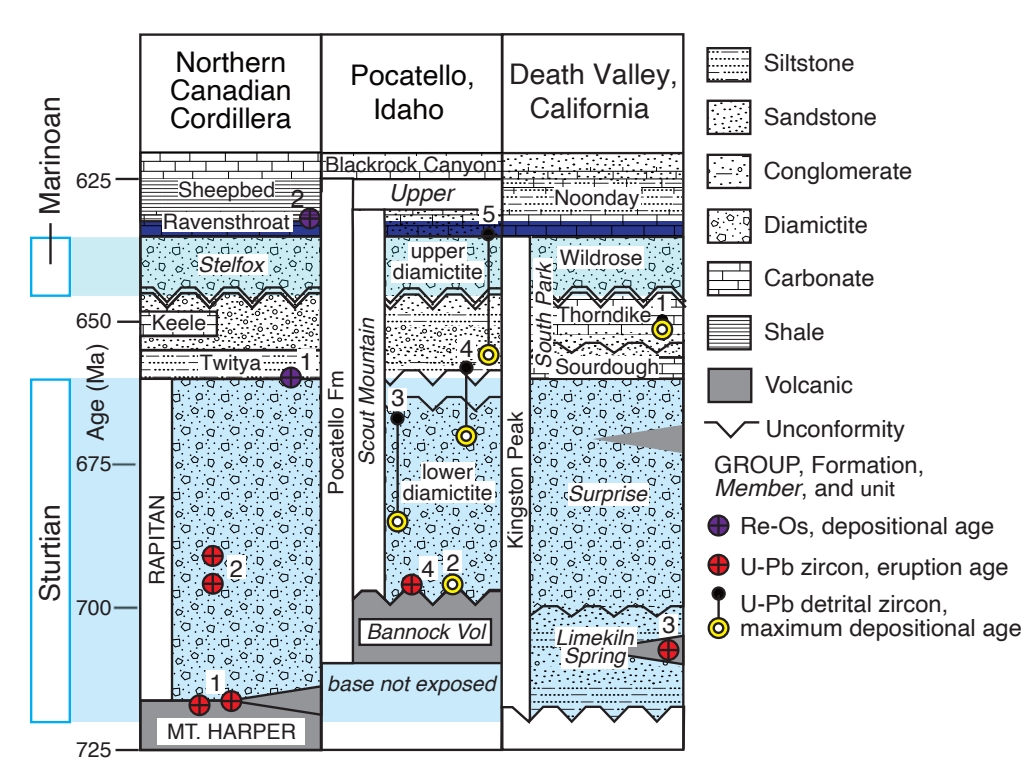


Figure 10. Correlation chart of late Neoproterozoic successions along the western margin of Laurentia. For detrital zircon maximum depositional ages, the position of the colored circle denotes the maximum depositional age with the black dot at the end of the connecting line signifying the general stratigraphic position of the sample. Simplified stratigraphic sections and general position of unconformities are modified from northern Canadian Cordillera (Rainbird et al., 1996; Macdonald et al., 2010, 2018; Rooney et al., 2014) and Death Valley, California, USA (Petterson et al., 2011, Macdonald et al., 2013a; Nelson et al., 2020). Geochronological constraints are summarized from Re-Os shale (1-Roonev et al., 2014; 2-Roonev et al., 2015); U-Pb zircon CA-IDTIMS (1-Macdonald et al., 2010; 2-Eyster et al., 2018; 3-Nelson et al. 2020: 4-this study): U-Pb detrital zircon maximum depositional age (1-Nelson et al., 2020; 2-this study; 3-Keeley et al., 2013; 4-this study; 5-this study), Fm - Formation; Vol - Volcanic,

here enhance the likelihood of this correlation of the upper diamictite and cap dolostone to the ≤650–635 Ma Marinoan glaciation and to lithologically similar deposits of this age throughout the Cordillera (Fig. 10).

CONCLUSIONS

The data presented here highlight the power of a tandem approach of in situ and CA-IDTIMS analytical techniques to accurately date zircon and establish clear age constraints on Neoproterozoic strata. Tandem analysis capitalizes on the strength of LA-ICPMS analysis for rapid identification of the youngest grains in a complex detrital zircon spectrum and on the ability of CA-IDTIMS to improve upon the precision and accuracy of the dates for the same grains. Additionally, this contribution reemphasizes previous conclusions of Condon and Bowring (2011) that encourage caution when attempting to construct age models and test global correlations with geochronological data of insufficient resolution to identify mixed epiclastic crystal ages or subtle Pb loss that bias the accuracy of U-Pb dates.

The ca. 696 Ma depositional age constraint from volcanic ash beds in the lower Scout Mountain Member of the Pocatello Formation confirms hypotheses (e.g., Macdonald et al., 2013a) that these strata are correlative with other dated Sturtian glacial deposits, e.g., the ca. 717-661 Ma Rapitan Group in Canada (Macdonald et al., 2010, 2018), the ≤719 Ma Hula Hula diamictite of Arctic Alaska (Cox et al., 2015), 705 Ma volcanics from the syn-glacial Kingston Peak Formation in Death Valley (Nelson et al., 2020), and ca. 697-690 Ma diamictite interbedded with the Gataga volcanics in northern British Columbia (Eyster et al., 2018). The base of the Pocatello Formation is fault bounded or in the subsurface; thus a parsimonious interpretation is that the preserved strata in the lower Scout Mountain Member and underlying Bannock Volcanic Member represent an interval of deposition during an extended Sturtian glacial event. The detrital zircon evidence of ca. 658-675 Ma zircon grains in overlying non-glacial marine shoreface sandstones, unconformably above the lower diamictite, does not refute the current model of Sturtian deglaciation at ca. 661 Ma (Zhou et al., 2019; Rooney et al., 2020).

A ca. 667 ± 5 Ma depositional age for the "reworked fallout tuff bed" of Fanning and Link (2004) has not been reproduced; rather, our sample of this unit contains a clear epiclastic detrital zircon age distribution with an abundant population of 675–673 Ma grains, which provides only a maximum depositional age. We show that this detrital zircon signal is essentially the same as that found throughout the Scout Mountain Member, including the marine shoreface sandstones above the disconformity developed on the lower diamictite. The recognition of epiclastic detrital zircon ranging to as young as 658 Ma in the upper diamictite further increases the probability that the upper diamictite—cap dolostone succession in the upper Scout Mountain Member is a product of the Marinoan glaciation. These findings remove one of the last counter-examples to the global correlation of the distinctive textural and isotopic properties of the Marinoan cap dolostone (Knoll et al., 2006; Dehler et al., 2011; Petterson et al., 2011).

ACKNOWLEDGMENTS

This work was supported by grants to MDS (U.S. National Science Foundation [NSF] grant EAR-1148499) and FAM (NSF grant EAR-1148058) for Cryogenian geochronology, and to MDS for LA-ICPMS and TIMS instrumentation at Boise State University (Murdock Charitable Trust and NSF grants EAR-1337887, EAR-0824974, EAR-0521221). We thank Paul Hoffman, Chris Holm-Denoma, Todd LaMaskin, two anonymous reviewers, and the editorial staff for thorough reading and constructive comments that greatly improved the final manuscript.

REFERENCES CITED

- Allen, C.M., and Campbell, I.H., 2012, Identification and elimination of a matrix-induced systematic error in LA-ICP-MS ²⁰⁸Pb/²³⁸U dating of zircon: Chemical Geology, v. 332–333, p. 157–165, https://doi.org/10.1016/j.chemgeo.2012.09.038.
- Balgord, E.A., Yonkee, W.A., Link, P.K., and Fanning, C.M., 2013, Stratigraphic, geochronologic, and geochemical record of the Cryogenian Perry Canyon Formation, northern Utah: Implications for Rodinia rifting and snowball Earth glaciation: Geological Society of America Bulletin, v. 125, p. 1442–1467, https://doi.org/10.1130/B30860.1.
- Bao, X., Zhang, S., Jiang, G., Wu, H., Li, H., Wang, X., An, Z., and Yang, T., 2018, Cyclostratigraphic constraints on the duration of the Datangpo Formation and the onset age of the Nantuo (Marinoan) glaciation in South China: Earth and Planetary Science Letters, v. 483, p. 52–63, https://doi.org/10.1016/j.epsl.2017.12.001.
- Bond, G.C., Kominz, M.A., and Devlin, W.J., 1983, Thermal subsidence and eustasy in the Lower Palaeozoic miogeocline of western North America: Nature, v. 306, p. 775–779, https://doi.org/10.1038/306775a0.
- Bowring, S.A., Grotzinger, J.P., Condon, D.J., Ramezani, J., Newall, M.J., and Allen, P.A., 2007, Geochronologic constraints on the chronostratigraphic framework of the Neoproterozoic Huqf Supergroup, Sultanate of Oman: American Journal of Science, v. 307, p. 1097–1145, https://doi.org/10.2475/10.2007.01.
- Budyko, M.I., 1969, The effect of solar radiation variations on the climate of the Earth: Tellus XXI, v. 5, p. 611–619.
- Calver, C.R., Crowley, J.L., Wingate, M.T.D., Evans, D.A.D., Raub, T.D., and Schmitz, M.D., 2013, Globally synchronous Marinoan deglaciation indicated by U-Pb geochronology of the Cottons Breccia, Tasmania, Australia: Geology, v. 41, p. 1127–1130, https://doi.org/10.1130/G34568.1.
- Cheel, R.J., and Leckie, D.A., 1993, Hummocky cross-stratification, in Wright, V.P., ed., Sedimentology Review/1: Oxford, UK, Blackwell Science, p. 103–122, https://doi.org/10.1002/9781444304534.ch7.
- Christie-Blick, N., 1983, Glacial-marine and subglacial sedimentation, Upper Proterozoic Mineral Fork Formation, Utah, in Molnia, B.F., ed., Glacial-Marine Sedimentation: New York, Plenum Press, p. 703–776, https://doi.org/10.1007/978-1-4613-3793-5_18.
- Colpron, M., Logan, J.M., and Mortensen, J.K., 2002, U-Pb zircon age constraint for late Neoproterozoic rifting and initiation of the lower Paleozoic passive margin of western Laurentia: Canadian Journal of Earth Sciences, v. 39, no. 2, p. 133–143, https://doi.org/10.1139/e01-069.
- Condon, D.J., and Bowring, S.A., 2011, A user's guide to Neoproterozoic geochronology, in Arnauld, E., Halverson, G.P., and Shields-Zhou, G., eds., The Geological Record of Neoproterozoic Glaciations: Geological Society of London Memoir 36, p. 135–149, https://doi.org/10.1144/M36.9.
- Condon, D., Zhu, M., Bowring, S., Wang, W., Yang, A., and Jin, Y., 2005, U-Pb ages from the Neoproterozoic Doushantuo Formation, China: Science, v. 308, p. 95–98, https://doi.org/10 1126/science 1107765
- Condon, D.J., Schoene, B., McLean, N.M., Bowring, S.A., and Parrish, R.R., 2015, Metrology and traceability of U-Pb isotope dilution geochronology (EARTHTIME Tracer Calibration Part I): Geochimica et Cosmochimica Acta, v. 164, p. 464–480, https://doi.org/10.1016/j.gca .2015.05.026.
- Cox, G.M., Strauss, J.V., Halverson, G.P., Schmitz, M.D., McClelland, W.D., Stevenson, R.S., and Macdonald, F.M., 2015, Kikiktat volcanics of Arctic Alaska—Melting of harzburgitic mantle associated with the Franklin large igneous province: Lithosphere, v. 7, p. 275–295, https:// doi.org/10.1130/L435.1.
- Cox, G.M., Isakson, V., Hoffman, P.F., Gernon, T.M., Schmitz, M.D., Shahin, S., Collins, A.S., Preiss, W., Blades, M.L., Mitchell, R.N., and Nordsvan, A., 2018, South Australian U-Pb zircon (CA-ID-TIMS) age supports globally synchronous Sturtian deglaciation: Precambrian Research, v. 315, p. 257–263, https://doi.org/10.1016/j.precamres.2018.07.007.

- Corsetti, F.A., Link, P.K., and Lorentz, N.J., 2007, δ¹ªC chemostratigraphy of the Neoproterozoic succession near Pocatello, Idaho, USA: Implications for glacial chronology and regional correlations, *in* Link, P.K., and Lewis, R.S., eds., Proterozoic Geology of Western North America and Siberia: SEPM Special Publication, no. 86, p. 193–205, https://doi.org/10.2110/pec.0786.0193.
- Crittenden, M.D., Jr., Schaeffer, F.E., Trimble, D.E., and Woodward, L.A., 1971, Nomenclature and correlation of some upper Precambrian and basal Cambrian sequences in western Utah and southeastern Idaho: Geological Society of America Bulletin, v. 82, p. 581–602, https://doi.org/10.1130/0016-7606(1971)82[581:NACOSU]2.0.CO;2.
- Crittenden, M.D., Jr., Christie-Blick, N., and Link, P.K., 1983, Evidence for two pulses of glaciation during the late Proterozoic in northern Utah and southeastern Idaho: Geological Society of America Bulletin, v. 94, p. 437–450, https://doi.org/10.1130/0016-7606(1983)94<437:EFTPOG>2 .0.CO:2.
- Dehler, C.M., Fanning, C.M., and Link, P.K., 2009, Getting better with age: New U-Pb SHRIMP data from the "Sturtian" Scout Mountain diamictite-cap-carbonate sequence, Pocatello Fm, Idaho: Geological Society of America Abstracts with Programs, v. 41, no. 7, p. 591.
- Dehler, C.M., Anderson, K., and Nagy, R., 2011, New descriptions of the cap dolostone and associated strata, Neoproterozoic Pocatello Formation, southeastern Idaho, USA, in Lee, J., and Evans, J.P., eds., Geologic Field Trips to the Basin and Range, Rocky Mountains, Snake River Plain, and Terranes of the U.S. Cordillera: Geological Society of America Field Guide 21, p. 183–194, https://doi.org/10.1130/2011.0021(08).
- Dickinson, W.R., 2006, Geotectonic evolution of the Great Basin: Geosphere, v. 2, p. 353–368, https://doi.org/10.1130/GES00054.1.
- Eisbacher, G.H., 1985, Late Proterozoic rifting, glacial sedimentation, and sedimentary cycles in the light of Windermere deposition, western Canada: Palaeogeography, Palaeoclimatology, Palaeoecology, v. 51, p. 231–254, https://doi.org/10.1016/0031-0182(85)90087-2.
- Evans, D.A.D., 2000, Stratigraphic, geochronological, and paleomagnetic constraints upon the Neoproterozoic climatic paradox: American Journal of Science, v. 300, p. 347–433, https://doi.org/10.2475/ajs.300.5.347.
- Evans, D.A.D., and Raub, T.D., 2011, Neoproterozoic glacial palaeolatitudes: A global update, in Arnaud, E., Halverson, G.P., and Shields-Zhou, G., eds., The Geological Record of Neoproterozoic Glaciations: Geological Society of London Memoir 36, p. 93–112, https://doi.org/10 1144/M36 7
- Eyster, A.E., Ferri, F., Schmitz, M.D., and Macdonald, F.A., 2018, One diamictite and two rifts: Stratigraphy and geochronology of the Gataga Mountain of northern British Columbia: American Journal of Science, v. 318, p. 167–207, https://doi.org/10.2475/02.2018.1.
- Fanning, C.M., and Link, P.K., 2004, U-Pb SHRIMP ages of Neoproterozoic (Sturtian) glacigenic Pocatello Formation, southeastern Idaho: Geology, v. 32, p. 881–884, https://doi.org/10.1130 /G20609.1.
- Fanning, C.M., and Link, P.K., 2008, Age constraints for the Sturtian glaciation: Data from the Adelaide Geosyncline, South Australia and Pocatello Formation, Idaho, USA, in Gallagher, S.J., and Wallace, M.W., eds., Selwyn Symposium 2008: Neoproterozoic Extreme Climates and the Evolution of Early Metazoan Life: Geological Society of Australia Extended Abstracts 91, p. 57–62.
- Fedo, C.M., and Cooper, J.D., 2001, Sedimentology and sequence stratigraphy of Neoproterozoic and Cambrian units across a craton-margin hinge zone, southeastern California, and implications for the early evolution of the Cordilleran margin: Sedimentary Geology, v. 141–142, p. 501–522, https://doi.org/10.1016/S0037-0738(01)00088-4.
- Halverson, G., Porter, S., and Shields, G., 2020, The Tonian and Cryogenian Periods, in Gradstein, F.M., Ogg, J.G., Schmitz, M.D., and Ogg, G.M., eds., Geologic Time Scale 2020: Amsterdam, Elsevier, v. 1, p. 495–519, https://doi.org/10.1016/B978-0-12-824360-2.00017-6.
- Harper, G.D., and Link, P.K., 1986, Geochemistry of Upper Proterozoic rift-related volcanics, northern Utah and southeastern Idaho: Geology, v. 14, p. 864–867, https://doi.org/10.1130/0091-7613 (1986)14<864:GOUPRV>2.0.CO;2.
- Hoffman, P.F., and Li, Z.-X., 2009, A palaeogeographic context for Neoproterozoic glaciation: Palaeogeography, Palaeoclimatology, Palaeoecology, v. 277, p. 158–172, https://doi.org/10.1016/j.palaeo.2009.03.013.
- Hoffman, P.F., and Schrag, D.P., 2002, The snowball Earth hypothesis: Testing the limits of global change: Terra Nova, v. 14, p. 129–155, https://doi.org/10.1046/j.1365-3121.2002.00408.x.
- Hoffman, P.F., Kaufman, A.J., Halverson, G.P., and Schrag, D.P., 1998, A Neoproterozoic snowball Earth: Science, v. 281, p. 1342–1346, https://doi.org/10.1126/science.281.5381.1342.
- Hoffman, P.F., Macdonald, F.A., and Halverson, G.P., 2011, Chemical sediments associated with Neoproterozoic glaciation: Iron formation, cap carbonate, barite and phosphorite, *in* Arnaud, E.,

- Halverson, G.P., and Shields-Zhou, G., eds., The Geological Record of Neoproterozoic Glaciations: Geological Society of London Memoir 36, p. 67–80, https://doi.org/10.1144/M36.5.
- Hoffman, P.F., Abbot, D.S., Ashkenazy, Y., Benn, D.I., Brocks, J.J., Cohen, P.A., Cox, G.M., Creveling, J.R., Donnadieu, Y., Erwin, D.H., Fairchild, I.J., Ferreira, D., Goodman, J.C., Halverson, G.P., Jansen, M.F., Le Hir, G., Love, G.D., Macdonald, F.A., Maloof, A.C., Partin, C.A., Ramstein, G., Rose, B.E.J., Rose, C.V., Sadler, P.M., Tziperman, E., Voigt, A., and Warren, S.G., 2017, Snowball Earth climate dynamics and Cryogenian geology-geobiology: Science Advances, v. 3, e1600983, https://doi.org/10.1126/sciadv.1600983.
- Hoffmann, K.H., Condon, D.J., Bowring, S.A., and Crowley, J.L., 2004, U-Pb zircon date from the Neoproterozoic Ghaub Formation, Namibia: Constraints on Marinoan glaciation: Geology, v. 32, p. 817–820, https://doi.org/10.1130/G20519.1.
- Horstwood, M.S.A., Košler, J., Gehrels, G., Jackson, S.E., McLean, N.M., Paton, C., Pearson, N.J., Sircombe, K., Sylvester, P., Vermeesch, P., Bowring, J.F., Condon, D.J., and Schoene, B., 2016, Community-derived standards for LA-ICP-MS U-(Th-)Pb geochronology Uncertainty propagation, age interpretation and data reporting: Geostandards and Geoanalytical Research, v. 40. p. 311–332. https://doi.org/10.1111/j.1751-908X.2016.00379.x.
- Jaffey, A.H., Flynn, K.F., Glendenin, L.E., Bentley, W.C., and Essling, A.M., 1971, Precision measurements of half-lives and specific activities of ²³⁶U and ²³⁸U: Physical Review C, v. 4, p. 1889–1906, https://doi.org/10.1103/PhysRevC.4.1889.
- Keeley, J.A., and Link, P.K., 2011, Middle Cryogenian ("Sturtian") Pocatello Formation: Field relations on Oxford Mountain and the Portneuf area, southeast Idaho, in Lee, J., and Evans, J.P., eds., Geologic Field Trips to the Basin and Range, Rocky Mountains, Snake River Plain, and Terranes of the U.S. Cordillera: Geological Society of America Field Guide 21, p. 165–180, https://doi.org/10.1130/2011.0021(07).
- Keeley, J.A., Link, P.K., Fanning, C.M., and Schmitz, M.D., 2013, Pre- to synglacial rift-related volcanism in the Neoproterozoic (Cryogenian) Pocatello Formation, SE Idaho: New SHRIMP and CA-ID-TIMS constraints: Lithosphere, v. 5. p. 128–150. https://doi.org/10.1130/L226.1.
- Kendall, B., Creaser, R.A., and Selby, D., 2006, Re-Os geochronology of postglacial black shales in Australia: Constraints on the timing of "Sturtian" glaciation: Geology, v. 34, p. 729–732, https://doi.org/10.1130/G22775.1.
- Kendall, B., Creaser, R.A., Calver, C.R., Raub, T.D., and Evans, D.A.D., 2009, Correlation of Sturtian diamictite successions in southern Australia and northwestern Tasmania by Re-Os black shale geochronology and the ambiguity of 'Sturtian'-type diamictite-cap carbonate pairs as chronostratigraphic marker horizons: Precambrian Research, v. 172, p. 301–310, https://doi .org/10.1016/j.precamres.2009.05.001.
- Kennedy, M.J., 1996, Stratigraphy, sedimentology, and isotopic geochemistry of Australian Neoproterozoic postglacial cap dolostones: Deglaciation, δ¹³C excursions, and carbonate precipitation: Journal of Sedimentary Research, v. 66, p. 1050–1064, https://doi.org/10.2110/jsr.66.1050.
- Kennedy, M.J., Runnegar, B., Prave, A.R., Hoffmann, K.H., and Arthur, A.A., 1998, Two or four Neoproterozoic glaciations?: Geology, v. 26, p. 1059–1063, https://doi.org/10.1130/0091-7613 (1998)026<1059:TOFNG>2.3.CO:2.
- Kirschvink, J.L., 1992, Late Proterozoic low-latitude glaciation: The snowball Earth, in Schopf, J.W., and Klein, C., eds., The Proterozoic Biosphere: A Multi-Disciplinary Study: New York, Cambridge University Press, p. 51–52.
- Knoll, A., Walter, M., Narbonne, G., and Christie-Blick, N., 2006, The Ediacaran Period: A new addition to the geologic time scale: Lethaia, v. 39, p. 13–30, https://doi.org/10.1080/00241160500409223.
- Krogh, T.E., 1973, A low-concentration method for hydrothermal decomposition of zircon and extraction of U and Pb for isotopic age determinations: Geochimica et Cosmochimica Acta, v. 37, p. 485–494, https://doi.org/10.1016/0016-7037(73)90213-5.
- Lan, Z., Li, X.-H., Zhang, Q., and Li, Q.-L., 2015, Global synchronous initiation of the 2nd episode of Sturtian glaciation: SIMS zircon U-Pb and O isotope evidence from the Jiangkou Group, South China: Precambrian Research, v. 267, p. 28–38, https://doi.org/10.1016/j.precamres.2015.06.002.
- Lan, Z., Huyskens, M.H., Lu, K., Li, X.-H., Zhang, G., Lu, D., and Yin, Q.-Z., 2020, Toward refining the onset age of Sturtian glaciation in South China: Precambrian Research, v. 338, 105555, https://doi.org/10.1016/j.precamres.2019.105555.
- Le Heron, D.P., Eyles, N., and Busfield, M.E., 2020, The Laurentian Neoproterozoic Glacial Interval: Reappraising the extent and timing of glaciation: Australian Journal of Earth Sciences, v. 113, p. 59–70, https://doi.org/10.17738/ajes.2020.0004.
- Levy, M., and Christie-Blick, N., 1991, Tectonic subsidence of the early Paleozoic passive continental margin in eastern California and southern Nevada: Geological Society of America Bulletin, v. 103, p. 1590–1606, https://doi.org/10.1130/0016-7606(1991)103<1590:TSOTEP>2.3.CO;2.

- Li, Z.X., Bogdanova, S.V., Collins, A.S., Davidson, A., De Waele, B., Ernst, R.E., Fitzsimons, L.C.W., Fuck, R.A., Gladkochub, D.P., Jacobs, J., Karlstrom, K.E., Lu, S., Natapov, L.M., Pease, V., Pisarevsky, S.A., Thrane, K., and Vernikovsky, V., 2008, Assembly, configuration, and breakup history of Rodinia: A synthesis: Precambrian Research, v. 160, p. 179–210, https://doi.org/10 .1016/j.precamres.2007.04.021.
- Link, P.K., 1982, Geology of the upper Proterozoic Pocatello Formation, Bannock Range, southeastern Idaho [Ph.D. thesis]: Santa Barbara, University of California, 131 p.
- Link, P.K., 1983, Glacial and tectonically influenced sedimentation in the Upper Proterozoic Pocatello Formation, southeastern Idaho, in Miller, D.M., Todd, V.R., and Howard, K.A., eds, Tectonic and Stratigraphic Studies in the Eastern Great Basin: Geological Society of America Memoir 157, p. 165–182, https://doi.org/10.1130/MEM157-p165.
- Link, P.K., and Christie-Blick, N., 2011, Neoproterozoic strata of southeastern Idaho and Utah: Record of Cryogenian rifting and glaciation, in Arnaud, E., Halverson, G.P., and Shields-Zhou, G., eds., The Geological Record of Neoproterozoic Glaciations: Geological Society of London Memoir 36, p. 425–436, https://doi.org/10.1144/M36.38.
- Link, P.K., Christie-Blick, N., Devlin, W.J., Elston, D.P., Horodyski, R.J., Levy, M., Miller, J.M.G., Pearson, R.C., Prave, A., Stewart, J.H., Winston, D., Wright, L.A., and Wrucke, C.T., 1993, Middle and Late Proterozoic stratified rocks of the western U.S. Cordillera, Colorado Plateau and Basin and Range province, in Reed, J.C., Jr., Bickford, M.E., Houston, R.S., Link, P.K., Rankin, D.W., Sims, P.K., and Van Schmus, W.R., eds., Precambrian: Conterminous U.S.: Boulder, Colorado, The Geological Society of America, The Geology of North America, v. C-2, p. 463–595, https://doi.org/10.1130/DNAG-GNA-C2.463.
- Link, P.K., Miller, J.M.G., and Christie-Blick, N., 1994, Glacial-marine facies in a continental rift environment: Neoproterozoic rocks of the western United States Cordillera, in Deynoux, M., Miller, J.M.G., Domack, E.W., Eyles, N., Fairchild, I., and Young, G.M., eds., Earth's Glacial Record: Cambridge, UK, Cambridge University Press, p. 29–46, https://doi.org/10.1017 /CBO9780511628900.003.
- Link, P.K., Corsetti, F.A., and Lorentz, N.J., 2005, Link, P.K., Corsetti, F.A., and Lorentz, N.J., 2005, Pocatello Formation and overlying strata, southeastern Idaho: Snowball Earth diamictites, cap carbonates, and Neoproterozoic isotopic profiles, in Pederson, J., and Dehler, C.M., eds., Interior Western United States: Geological Society of America Field Guide 6, p. 251–259, https://doi.org/10.1130/2005.fl d006(12).
- Lorentz, N.J., Corsetti, F.A., and Link, P.K., 2004, Seafloor precipitates and C isotope stratigraphy from the Neoproterozoic Scout Mountain Member of the Pocatello Formation, southeast Idaho: Implications for Neoproterozoic Earth system behavior: Precambrian Research, v. 130, p. 57–70, https://doi.org/10.1016/j.precamres.2003.10.017.
- Lund, K., Aleinikoff, J.N., Evans, K.V., and Fanning, C.M., 2003, SHRIMP U-Pb geochronology of Neoproterozoic Windermere Supergroup, central Idaho: Implications for rifting of western Laurentia and synchroneity of Sturtian glacial deposits: Geological Society of America Bulletin, v. 115, p. 349–372, https://doi.org/10.1130/0016-7606(2003)115<0349:SUPGON>2.0.CC;2.
- Lund, K., Aleinikoff, J.N., and Evans, K.V., 2011, The Edwardsburg Formation and related rocks, Windermere Supergroup, central Idaho, USA, in Arnaud, E., Halverson, G.P., and Shields-Zhou, G., eds., The Geological Record of Neoproterozoic Glaciations: Geological Society of London Memoir 36, p. 437–448, https://doi.org/10.1144/M36.39.
- Macdonald, F.A., Schmitz, M.D., Crowley, J.L., Roots, C.F., Jones, D.S., Maloof, A.C., Strauss, J.V., Cohen, P.A., Johnston, D.T., and Schrag, D.P., 2010, Calibrating the Cryogenian: Science, v. 327, p. 1241–1243, https://doi.org/10.1126/science.1183325.
- Macdonald, F.A., Prave, A.R., Petterson, R., Smith, E.F., Pruss, S.B., Oates, K., Waechter, F., Trotzuk, D., and Fallick, A.E., 2013a, The Laurentian record of Neoproterozoic glaciation, tectonism, and eukaryotic evolution in Death Valley, California: Geological Society of America Bulletin, v. 125, p. 1203–1223, https://doi.org/10.1130/B30789.1.
- Macdonald, F.A., Strauss, J.V., Sperling, E.A., Halverson, G.P., Narbonne, G.M., Johnston, D.T., Kunzmann, M., Schrag, D.P., and Higgins, J.A., 2013b, The stratigraphic relationship between the Shuram carbon isotope excursion, the oxygenation of Neoproterozoic oceans, and the first appearance of the Ediacara biota and bilaterian trace fossils in northwestern Canada: Chemical Geology, v. 362, p. 250–272, https://doi.org/10.1016/j.chemgeo.2013.05.032.
- Macdonald, F.A., Schmitz, M.D., Strauss, J.V., Halverson, G.P., Gibson, T.M., Eyster, A., Cox, G., Mamrol, P., and Crowley, J.L., 2018, Cryogenian of Yukon: Precambrian Research, v. 319, p. 114–143, https://doi.org/10.1016/j.precamres.2017.08.015.
- MacLennan, S., Park, Y., Swanson-Hysell, N., Maloof, A., Schoene, B., Gebreslassie, M., Antilla, E., Tesema, T., Alene, M., and Haileab, B., 2018, The arc of the Snowball: U-Pb dates constrain

- the Islay anomaly and the initiation of the Sturtian glaciation: Geology, v. 46, p. 539–542, https://doi.org/10.1130/G40171.1.
- Mattinson, J.M., 2005, Zircon U-Pb chemical abrasion ("CA-TIMS") method: Combined annealing and multi-step partial dissolution analysis for improved precision and accuracy of zircon ages: Chemical Geology, v. 220, p. 47–66, https://doi.org/10.1016/j.chemgeo.2005.03.011.
- McLean, N.M., Condon, D.J., Schoene, B., and Bowring, S.A., 2015, Evaluating uncertainties in the calibration of isotopic reference materials and multi-element isotopic tracers (EARTHTIME Tracer Calibration Part II): Geochimica et Cosmochimica Acta, v. 164, p. 481–501, https://doi.org/10.1016/j.gca.2015.02.040.
- Michel, L.A., Schmitz, M.D., Tabor, N.J., Montañez, I.P., and Davydov, V.I., 2016, Reply to the comment on "Chronostratigraphy and paleoclimatology of the Lodève Basin, France: Evidence for a pan-tropical aridification event across the Carboniferous-Permian boundary" by Michel et al., (2015). Paleogeography, Palaeoclimatology, Palaeoecology 430, 118–131: Palaeogeography, Palaeoclimatology, Palaeoecology, v. 441, p. 1000–1004, https://doi.org/10.1016/j.palaeo.2015.10.023.
- Moynihan, D.P., Strauss, J.V., Nelson, L.L., and Padget, C.D., 2019, Upper Windermere Super-group and the transition from rifting to continent-margin sedimentation, Nadaleen River area, northern Canadian Cordillera: Geological Society of America Bulletin, v. 131, p. 1673–1701, https://doi.org/10.1130/B32039.1.
- Nasdala, L., Lengauer, C.L., Hanchar, J.M., Kronz, A., Wirth, R., Blanc, P., Kennedy, A.K., and Seydoux-Guillaume, A.-M., 2002, Annealing radiation damage and the recovery of cathodoluminescence: Chemical Geology, v. 191, p. 121–140, https://doi.org/10.1016/S0009-2541 (02)00152-3.
- Nelson, L.L., Smith, E.F., Hodgin, E.B., Crowley, J.L., Schmitz, M.D., and Macdonald, F.A., 2020, Geochronological constraints on Neoproterozoic rifting and onset of the Marinoan glaciation from the Kingston Peak Formation in Death Valley, California (USA): Geology, v. 48, p. 1083–1087, https://doi.org/10.1130/G47668.1.
- North, G.R., Cahalan, R.F., and Coakley, J.A., Jr, 1981, Energy balance climate models: Reviews of Geophysics and Space Physics, v. 19, p. 91–121.
- Petterson, R., Prave, A.R., Wernicke, B.P., and Fallick, A.E., 2011, The Neoproterozoic Noonday Formation, Death Valley Region, California: Geological Society of America Bulletin, v. 123, p. 1317–1336, https://doi.org/10.1130/B30281.1.
- Pigage, L.C., and Mortensen, J.K., 2004, Superimposed Neoproterozoic and early Tertiary alkaline magmatism in the La Biche River area, southeast Yukon Territory: Bulletin of Canadian Petroleum Geology, v. 52, no. 4, p. 325–342.
- Platt, L.B., 1998, Geologic map of the Scout Mountain quadrangle, Bannock County, Idaho: Idaho Geological Survey, Geologic Map GM-22, scale 1:24,000.
- Prave, A.R., 1999, Two diamictites, two cap carbonates, two δ¹³C excursions, two rifts: The Neoproterozoic Kingston Peak Formation, Death Valley, California: Geology, v. 27, p. 339–342, https://doi.org/10.1130/0091-7613(1999)027<0339:TDTCCT>2.3.CO;2.
- Prave, A.R., Condon, D.J., Heinz-Hoffmann, K., Tapster, S., and Fallick, A.E., 2016, Duration and nature of the end-Cryogenian (Marinoan) glaciation: Geology, v. 44, p. 631–634, https://doi.org/10.1130/G38089.1.
- Rainbird, R.H., Jefferson, C.W., and Young, G.M., 1996, The early Neoproterozoic sedimentary Succession B of northwestern Laurentia: Correlations and paleogeographic significance: Geological Society of America Bulletin, v. 108, no. 4, p. 454–470, https://doi.org/10.1130/0016 -7606(1996)108-0454:TENSSB>2.3.CO;2.
- Rivera, T.A., Storey, M., Schmitz, M.D., and Crowley, J.L., 2013, Age intercalibration of ⁴⁰Ar/³⁹Ar sanidine and chemically distinct U/Pb zircon populations from the Alder Creek Rhyolite Quaternary geochronology standard: Chemical Geology, v. 345, p. 87–98, https://doi.org/10.1016/j.chemgeo.2013.02.021.
- Rodgers, D.W., Long, S.P., McQuarrie, N.N., Burgel, W.D., and Hersley, C.F., 2006, Geologic Map of the Inkom Quadrangle, Bannock County, Idaho: Idaho Geological Survey, Technical Report T-06-2, scale 1:24,000.
- Rooney, A.D., Macdonald, F.A., Strauss, J.V., Dudás, F.Ö., Hallmann, C., and Selby, D., 2014, Re-Os geochronology and coupled Os-Sr isotope constraints on the Sturtian snowball Earth: Proceedings of the National Academy of Sciences of the United States of America, v. 111, p. 51–56, https://doi.org/10.1073/pnas.1317266110.
- Rooney, A.D., Strauss, J.V., Brandon, A.D., and Macdonald, F.A., 2015, A Cryogenian chronology: Two long-lasting synchronous Neoproterozoic glaciations: Geology, v. 43, p. 459–462, https://doi.org/10.1130/G36511.1.

- Rooney, A.D., Yang, C., Condon, D.J., Zhu, M., and Macdonald, F.A., 2020, U-Pb and Re-Os geochronology tracks stratigraphic condensation in the Sturtian snowball Earth aftermath: Geology, v. 48, p. 625–629, https://doi.org/10.1130/G47246.1.
- Ross, G.M., 1991, Tectonic setting of the Windermere Supergroup revisited: Geology, v. 19, p. 1125–1128. https://doi.org/10.1130/0091-7613(1991)019<1125:TSOTWS>2.3.CO:2.
- Schmitz, M.D., and Schoene, B., 2007, Derivation of isotope ratios, errors, and error correlations for U-Pb geochronology using ²⁰⁵Pb-²³⁵U-(²³³U)-spiked isotope dilution thermal ionization mass spectrometric data: Geochemistry Geophysics Geosystems, v. 8, Q08006, https://doi .org/10.1029/2006GC001492.
- Sláma, J., Kosler, J., Condon, D., Crowley, J., Gerdes, A., Hanchar, J., Horstwood, M., Morris, G., Nasdala, L., and Norberg, N., 2008, Plesovice zircon—A new natural reference material for U-Pb and Hf isotopic microanalysis: Chemical Geology, v. 249, p. 1–35.
- Spence, G.H., Le Heron, D.P., and Fairchild, I.J., 2016, Sedimentological perspectives on climatic, atmospheric and environmental change in the Neoproterozoic Era: Sedimentology, v. 63, p. 253–306, https://doi.org/10.1111/sed.12261.
- Vermeesch, P., Resentini, A., and Garzanti, E., 2016, An R package for statistical provenance analysis: Sedimentary Geology, v. 336, p. 14–25, https://doi.org/10.1016/j.sedgeo.2016.01.009.
- Walker, J.C.G., Hays, P.B., and Kasting, J.F., 1981, A negative feedback mechanism for the long-term stabilization of Earth's surface temperature: Journal of Geophysical Research, v. 86, p. 9776–9782, https://doi.org/10.1029/JC086iC10p09776.

- Wang, D., Zhu, X.-K., Zhao, N., Yan, B., Li, X.-H., Shi, F., and Zhang, F., 2019, Timing of the termination of Sturtian glaciation: SIMS U-Pb zircon dating from South China: Journal of Asian Earth Sciences, v. 177, p. 287–294, https://doi.org/10.1016/j.jseaes.2019.03.015.
- Wendt, I., and Carl, C., 1991, The statistical distribution of the mean squared weighted deviation: Chemical geology. Isotope geoscience section, v. 86, p. 275–285, https://doi.org/10.1016/0168-9622(91)90010-T.
- Williams, G.E., 1979, Sedimentology, stable-isotope geochemistry and palaeoenvironment of dolostones capping late Precambrian glacial sequences in Australia: Journal of the Geological Society of Australia, v. 26, p. 377–386, https://doi.org/10.1080/00167617908729104.
- Yonkee, W.A., Dehler, C.D., Link, P.K., Balgord, E.A., Keeley, J.A., Hayes, D.S., Wells, M.L., Fanning, C.M., and Johnston, S.M., 2014, Tectono-stratigraphic framework of Neoproterozoic to Cambrian strata, west-central U.S.: Protracted rifting, glaciation, and evolution of the North American Cordilleran margin: Earth-Science Reviews, v. 136, p. 59–95, https://doi.org/10.1016/j.earscirev.2014.05.004.
- Zhang, S., Jiang, G., and Han, Y., 2008, The age of the Nantuo Formation and Nantuo glaciation in South China: Terra Nova, v. 20, p. 289–294, https://doi.org/10.1111/j.1365-3121.2008.00819.x.
- Zhou, C., Tucker, R., Xiao, S., Peng, Z., Yuan, X., and Chen, Z., 2004, New constraints on the ages of Neoproterozoic glaciations in south China: Geological Society of America, v. 32, p. 437–440, https://doi.org/10.1130/G20286.1.
- Zhou, C., Huyskens, M.H., Lang, X., Xiao, S., and Yin, Q.-Z., 2019, Calibrating the terminations of Cryogenian global glaciations: Geology, v. 47, p. 251–254, https://doi.org/10.1130/G45719.1.